A 3D Moment of Fluid method for simulating complex turbulent multiphase flows

Anirudh Asuri Mukundan, Thibaut Ménard, Jorge César C Brändle de Motta, Alain Berlemont

A 3D Moment of Fluid method for simulating complex turbulent multiphase flows

Anirudh Asuri Mukundan[a,*], Thibaut Ménard[a,b], Jorge César Brändle de Motta[a,b], Alain Berlemont[a]

[a] *CNRS UMR6614 CORIA, Saint-Étienne-du-Rouvray, France*
[b] *Université de Rouen Normandie, Saint-Étienne-du-Rouvray, France*

Abstract

This paper presents the moment of fluid method as a liquid/gas interface reconstruction method coupled with a mass momentum conservative approach within the context of numerical simulations of incompressible two-phase flows. This method tracks both liquid volume fraction and phase centroid for reconstructing the interface. The interface reconstruction is performed in a volume (and mass) conservative manner and accuracy of orientation of interface is ensured by minimizing the centroid distance between original and reconstructed interface. With two-phase flows, moment of fluid method is able to reconstruct interface without needing phase volume data from neighboring cells. The performance of this method is analyzed through various transport and deformation tests, and through simple two-phase flows tests that encounter changes in the interface topologies. Exhaustive mesh convergence study for the reconstruction error has been performed through various transport and deformation tests involving simple two-phase flows. It is then applied to simulate atomization of turbulent liquid diesel jet injected into a quiescent environment. The volume conservation error for the moment of fluid method remains small for this complex turbulent case.

Keywords: Incompressible flow, DNS, Primary atomization, Multiphase flow, Moment of fluid, Mass conservation

*Corresponding author
Email addresses: anirudh.mukundan@coria.fr (Anirudh Asuri Mukundan), thibaut.menard@coria.fr (Thibaut Ménard)

1. Motivation and Objectives

Multiphase flows are ubiquitous in nature that are encountered in applications ranging from weather forecast to aircraft engines. In gas turbines and aircraft engines, the liquid fuel introduced in combustion chamber undergoes atomization, evaporation, mixing with the oxidizer, and subsequently combustion. Atomization process of the liquid fuel has a direct impact on the efficiency of combustion and amount of pollutants produced as by-products of combustion. This multiphase flow process is, by its nature, multi-scale. Consequently, with the current supercomputing facilities, the available numerical methods, and tools are not large enough to perform detailed predictive numerical simulations of the liquid fuel atomization for typical aircraft engine combustion chamber geometry.

The main challenge in performing multiphase flow simulations is the ability of the numerical method to handle change in fluid properties across the interface. For example, the density ratio between the fuel and air can be as high as 600 in aircraft engines and the methods should be able to handle it with least error. The bottleneck with such conditions is the discretization of Navier-Stokes equations. A force due to surface tension exists between the phases due to the nature of multiphase flows. This force acts only on the interface separating the phases. The challenge for the numerical method is to handle the singular nature of this force. Its computation can be difficult as the information about interface curvature is a prerequisite. Next, reconstruction and transport of the interface between the phases pose a challenge to these numerical methods and tools. The accuracy of the interface capture and transport has a direct impact on conservation of mass and stability of the solution of the Navier-Stokes equations and has been one of the main topics of extensive research in the numerical atomization research community [1]. Finally, the liquid fuel atomization process can generate droplets of varying sizes and scales. It is this multi-scale nature of atomization process requiring high resolution for the numerical simulations increases the computational expense. Of these challenges for numerical simulations of multiphase flows, this work addresses the development of accurate liquid/gas interface reconstruction and transport method.

Many interface capturing methods have been developed over the past decades, the prominent being volume of fluid (VOF) method [2, 3, 4]. The mass conservation is ensured in this method since the interface is represented by liquid volume fraction as scalar quantity. Due to its discontinuity across

the interface, the advection requires accurate numerical schemes [5]. Variety of the VOF based methods exists (see for example, [6, 7, 8, 9]) that improves the different limitations of the original VOF method.

Another class of family of methods for interface reconstruction is level set based methods [10, 11]. This method implicitly represents the interface as a zero level isocontour of a signed distance function. Such a representation has a considerable advantage in computing the geometrical quantities such as interface curvature. This method, in a way, paves way for the solution of the computation of the surface tension force as described above. This smooth implicit function can be maintained as signed distance function through a simple re-initialization process. Furthermore, the parallellization of the code is straightforward and the transport of this level set function can be performed using a simple Eulerian transport equation. Therefore, more accurate numerical schemes can be used for the discretization of this transport equation. Although this method proves to be robust, it is affected by the loss of mass. Multiple variations and improvements have been made to alleviate this issue. For example, the accurate conservative level set (ACLS) method [12, 13, 14] uses a tangent hyperbolic profile for the representation of the level set function and re-initialized using conservative equations. An alternative approach is local mesh refinement to increase the accuracy such as adaptive mesh refinement (AMR), refined level set grid (RLSG) method [15]. In RLSG method, the Navier-Stokes equations are solved on a coarser mesh while the level set function is transported on a finer mesh. Finally, the mass conservation property of the level set family of methods can be achieved by coupling with VOF method resulting in coupled level set volume of fluid method (CLSVOF) method [16, 17, 18]. In this method, the interface is reconstructed using the sharp level set function while the mass conservation is ensured by using the liquid volume fraction that is correcting the level set function.

Although these improved methods have proved to be useful in simulating multiphase flows, they can still fail in the computation of geometrical properties especially for under-resolved interface topologies [17]. One of the ways to accurately capture the under-resolved interfacial ligaments was demonstrated by Ahn and Shashkov [19] using the moment of fluid (MOF) method [20]. MOF method was introduced by Dyadechko and Shashkov [20] as an extension to the VOF method by *additionally* using the phase centroid for the interface reconstruction. Originally, this method was developed for finding optimal multi-material partitions [21, 22]. Recently, Jemison et al. [23], Li

et al. [24], Asuri Mukundan et al. [25, 26, 27] applied this method to multiphase flows simulations. Various implementations to the MOF method have been made in the past years, for example, Freiss et al. [28] extended this method to cylindrical coordinates for simulating axisymmetric flows, Galera et al. [29] and Breil et al. [30] applied the numerical method for arbitrary Lagrangian Eulerian (ALE) meshes. A notable improvement to the MOF interface reconstruction method was presented by Lemoine et al. [31] in which an analytical approach to reconstruct the interface was introduced thereby avoiding the geometric approach. Further to the ability of MOF method to capture under-resolved interfacial regions, it is imperative to know the convergence of the error in interface reconstruction. This information is required to have a first-hand knowledge of the optimal mesh resolution to be employed in simulating engineering fuel injection scenarios, for example simulating fuel injection in diesel and aircraft engines. In the study by Jemison et al. [23] multiple tests and mesh convergence analyses were performed, but the errors were reported only for coarse mesh resolutions.

In this work, we study the MOF method for its accuracy in interface reconstruction through multiple tests and investigated the mesh convergence of the error in reconstruction for mesh resolutions that are comparable to those generally employed for simulating primary atomization. Moreover, we have coupled our MOF method with our in-house solver ARCHER [17, 32, 33] that uses ghost fluid method (GFM) for the computation of surface tension force and that computes mass ad momentum flux consistently [33]. It is to be remarked that the MOF method presented in this paper is mainly intended to augment the consistent mass and momentum flux computation feature available in ARCHER for simulating atomization applications. Thus, no significant improvements in the liquid/gas interface reconstruction method has been made within the context of MOF interface reconstruction and advection methods in comparison to that presented in the works of Dyadechko and Shashkov [20], Jemison et al. [23].

This paper is organized as follows. Section 2 presents the Navier-Stokes equations and transport equations for the liquid volume fraction and level set fucntion. Section 3 presents the numerical method of moment of fluid (MOF) - the procedure employed for the interface reconstruction and transport. This is followed by the presentation of verification tests in Section 4 that reports the error in reconstruction. In these tests, we compare results from MOF method to those from CLSVOF method of Ménard et al. [17]. Section 5 then presents the solution procedure employed for solving the Navier-Stokes equa-

tions, GFM method, formulation of viscous term, and the time integration scheme used in our flow solver. Section 6 focus on validation tests with the presentation of simulations of convection dominated double shear layer and Rayleigh-Taylor instability test for assessing the accuracy of MOF method. Finally, Section 7 present the results from the simulation of atomization of turbulent liquid diesel jet.

2. Governing equations

2.1. Incompressible Navier–Stokes equations

To describe the multiphase flows, the pressure and velocity fields describing the flow are obtained by solving the incompressible Navier–Stokes equations. The following conservative form of the equations are solved in our flow solver [33]:

$$\boldsymbol{\nabla} \cdot \boldsymbol{u} = 0, \tag{1}$$

$$\frac{\partial \rho \boldsymbol{u}}{\partial t} + \boldsymbol{\nabla} \cdot (\rho \boldsymbol{u} \otimes \boldsymbol{u}) = -\boldsymbol{\nabla} P + \boldsymbol{\nabla} \cdot (2\mu \boldsymbol{D}) + \boldsymbol{B}, \tag{2}$$

where $\boldsymbol{u}$ is the velocity field, P is the pressure field, μ is dynamic viscosity, ρ is density, $\boldsymbol{D}$ is the strain rate tensor given as $\boldsymbol{D} = \frac{1}{2}(\boldsymbol{\nabla u} + (\boldsymbol{\nabla u})^T)$, and $\boldsymbol{B}$ is the sum of the body and surface tension forces. $\boldsymbol{B} = \boldsymbol{B}_{\mathrm{b}} + \boldsymbol{B}_{\mathrm{st}}$ where $\boldsymbol{B}_{\mathrm{b}}$ is the force due to gravity and $\boldsymbol{B}_{\mathrm{st}}$ is the force due to surface tension which is given as $\boldsymbol{B}_{\mathrm{st}} = \sigma\kappa\delta_I \boldsymbol{n}$. σ represent the surface tension, κ is the curvature of the interface computed using the level set function ϕ in our solver as

$$\kappa(\phi) = -\nabla \cdot \left(\frac{\nabla \phi}{\|\nabla \phi\|_2} \right), \tag{3}$$

and δ_I is the Dirac delta function centered on surface of the interface. In this work, we neglect effect due to gravity unless explicitly specified.

Within the context of two-phase flows, an interface Γ separates the liquid from the gaseous phase. The material properties are constant in each phase, i.e., $\rho = \rho_{\mathrm{liq}}$ and $\mu = \mu_{\mathrm{liq}}$ in liquid phase and $\rho = \rho_{\mathrm{gas}}$ and $\mu = \mu_{\mathrm{gas}}$ in gaseous phase. At the interface, these properties are subject to a jump that can be written as $[\rho]_\Gamma = \rho_{\mathrm{liq}} - \rho_{\mathrm{gas}}$ and $[\mu]_\Gamma = \mu_{\mathrm{liq}} - \mu_{\mathrm{gas}}$. The velocity field remain continuous across the interface, hence $[\boldsymbol{u}]_\Gamma = 0$. However, the pressure is not continuous across the interface and it is possible to write the pressure jump [17] as

$$[P]_\Gamma = \sigma\kappa(\phi) + 2[\mu]_\Gamma (\nabla \boldsymbol{u} \cdot \boldsymbol{n}) \cdot \boldsymbol{n}, \tag{4}$$

where $\boldsymbol{n}$ is the interface unit normal.

2.2. Volume fraction equation

Liquid volume fraction F within this work is defined as

$$F(\boldsymbol{x},t) = \frac{1}{\mid C_\Omega \mid} \int_{C_\Omega} H(\phi(\boldsymbol{x}),t) d\boldsymbol{x} \tag{5}$$

where H is the Heaviside function expressed as

$$H(\phi(\boldsymbol{x})) = \begin{cases} 1, & \text{if } \phi(\boldsymbol{x}) > 0 \\ 0, & \text{otherwise} \end{cases} \tag{6}$$

with the sign convention of then level set function ϕ taken as

$$\phi(\boldsymbol{x}) = \begin{cases} > 0, & \text{if } \boldsymbol{x} \text{ is inside liquid phase} \\ < 0, & \text{if } \boldsymbol{x} \text{ is inside gas phase,} \end{cases} \tag{7}$$

and C_Ω represents a computational cell in the numerical simulation domain Ω. Thus, F obey the bounds of $0 \leq F \leq 1$. The gaseous phase volume fraction is given as $1 - F$. The density is then computed using the liquid volume fraction as follows.

$$\rho(\boldsymbol{x}) = \rho_{\text{liq}} F + \rho_{\text{gas}}(1 - F) \tag{8}$$

Within this work, liquid volume fraction is considered as a passive scalar and hence its transport equation is given as

$$\frac{\partial F}{\partial t} + \nabla \cdot (F\boldsymbol{u}) = 0. \tag{9}$$

A directionally split advection technique following the algorithm presented in Weymouth and Yue [34] is employed for solving Equation (9). The advection directions are swapped alternatively between the adjacent time steps, i.e.,

$$\begin{aligned} t^n \rightarrow t^{n+1} &: x - y - z \\ t^{n+1} \rightarrow t^{n+2} &: y - z - x \\ t^{n+2} \rightarrow t^{n+3} &: z - x - y \\ &\text{repeat.} \end{aligned} \tag{10}$$

The following modified form of the transport equation consistent to the algorithm of Weymouth and Yue [34] is solved.

$$\frac{\partial F}{\partial t} + \boldsymbol{\nabla} \cdot (F\boldsymbol{u}) = c\,(\boldsymbol{\nabla} \cdot \boldsymbol{u}); \quad c = \begin{cases} 1, & F > 0.5 \\ 0, & \text{otherwise.} \end{cases} \tag{11}$$

The dilatation term $\boldsymbol{\nabla} \cdot \boldsymbol{u}$ appears in this equation due to the usage of operator split method of advection. In each step of this directionally split algorithm, the liquid volume fraction is advected along a one-dimensional flow which *is not divergence free*. Hence without this term, there will be *jetsam* and *floatsam* in the flow. Moreover, the bounds of $0 \leq F \leq 1$ cannot be maintained otherwise. It is to be remarked that by using the algorithm of Weymouth and Yue [34], there is no loss of liquid volume in the domain.

2.2.1. Level set function

Level set (LS) function ϕ within this work is considered as a passive scalar variable that is used for three purposes: 1) initialization of phase interface using which initial liquid volume in the domain is computed; 2) computation of interface curvature; and 3) representation of liquid gas interface results shown in Sections 4 and 7. It is advected using the same transport equation and advection scheme as that of liquid volume fraction (c.f. Equation (9)) [17].

2.2.2. Coupling level set with volume of fluid

To ensure that an accurate measure of level set is maintained in the simulation, care is taken in correcting the level set signed distance function based on the liquid volume fraction in each computational cell. This way, the computation of the interface curvature is not affected. Moreover, the re-initialization of level set function is performed as decribed by Ménard et al. [17]. The implementation of the level set advection, correction and coupling with VOF method is performed similar to a classical CLSVOF method as described Ménard et al. [17]; details of it are not recalled here.

Quite often numerical simulations of atomization process produces very small unphysical liquid structures in the domain. Such structures are, in general, under-resolved in the simulation domain. Our solver has the option to remove these structures from the domain and this process is carried out using level set function ϕ. The criteria for the removal is that, when there is no change in the sign of ϕ between a computational cell and all its neighbours, any liquid volume present in this cell is deleted. This process is called *VOF restriction* in our solver. It is possible to switch on or off the capture of these small structures. When these under-resolved liquid structures are not reconstructed accurately, it can have a detrimental effect on the stability of the solution of the Navier-Stokes equations. It is important to not remove these structures but also to maintain stability of the solution. It is for tackling

this quintessential issue, the proposed MOF method is developed. More information on the significance and application of this *VOF restriction*, the reader is referred to Section 6.1.

3. Moment of Fluid method

3.1. Original method

The original moment of fluid (MOF) method of Dyadechko and Shashkov [20] and Ahn and Shashkov [19] aims at finding the partitions of different materials in the context of multi-material applications containing M materials. According to Dyadechko and Shashkov [20], in order to find the divisional layout of the various materials, it was necessary to know the proximity of their partitions and to know the approximate mixed cell partitions that are of interest. To this end, they used VOF method to detect and reconstruct the partitions/interfaces between the different materials and used the material centroids to accurately orient the interface in a volume conservative manner. In finding the correct orientation of the reconstructed interface, the centroid defect, i.e., the distance between the material centroids of reconstructed and original interfaces had been used as a criterion for selection of the best orientation. In order to find the interested choice of the mixed cell partitions, the order in which material interfaces to be reconstructed was required. They determined the right order by trying all the $M!$ possible combinations and chosen the one with the least centroid defect.

With this solution procedure for finding the interfaces among various materials, Dyadechko and Shashkov [20] and Ahn and Shashkov [19] observed good mass conservation and also observed at least second-order of convergence of the interface reconstruction error metrics in comparison to the classical VOF and level set (LS) based approaches.

3.2. Interface normal computation

MOF method is a superset of the classical VOF method. MOF method tracks both liquid volume fraction (zeroth moment of liquid volume) and phase centroids (first moment of liquid volume) in each mixed computational cell (cell with liquid volume fraction value between 0 and 1) in order to numerically reconstruct the interface. As described by Dyadechko and Shashkov [20], we need these two information in order to reconstruct the

material interfaces. Within this work, we define the liquid phase volume fraction and phase centroid or center of mass (COM) respectively as

$$F = \frac{\int_\omega d\boldsymbol{x}}{\int_\Omega d\boldsymbol{x}}, \tag{12}$$

$$\boldsymbol{x}_{\mathrm{COM}} = \frac{\int_\omega \boldsymbol{x} d\boldsymbol{x}}{\int_\Omega d\boldsymbol{x}}, \tag{13}$$

where F represent liquid volume fraction, $\boldsymbol{x}_{\mathrm{COM}}$ is the liquid phase centroid/center of mass, and ω is the domain of the liquid packet (with its volume denoted by $\mid \omega \mid$) inside the computational cell C_Ω (with its volume denoted by $\mid C_\Omega \mid$). In the rest of this paper, the phase COM will be referred as *phase centroid*. For the computation of centroid in Equation (13), the reader is referred to Appendix A. The availability of liquid volume fraction and phase centroid establishes a self-sufficiency of the required information to reconstruct the approximate interface in a cell, thus, eradicating data requirement from the neighboring cells. The consequence of this property is a uniform treatment of the internal and boundary cells in the mesh thus, yielding the resolution of the interface as high as the computational mesh itself. It has been shown [19, 20] that MOF method reconstructs the linear interfaces exactly, thus, it is second-order accurate.

3.2.1. Problem formulation

Within the context of this work, MOF method is developed as a piecewise linear interface calculation (PLIC) method for reconstructing the interface. Thus, the equation of the reconstructed interface plane in 3D (line in 2D) is given as $ax+by+cz+d=0$ where interface normal $\boldsymbol{n} = [a, b, c]^T$. The reconstruction of original/reference interface means determining the components of interface normal $\boldsymbol{n}$ and shortest distance d of interface from cell center. This is carried out as the solution to a constrained optimization problem wherein both $\boldsymbol{n}$ and d have to be simultaneously determined such that volume is conserved (Equation (14)) and centroid defect E^{MOF} is minimized (Equation (15))

$$\left|F^{\mathrm{ref}} - F^{\mathrm{act}}(\boldsymbol{n}, d)\right| = 0, \text{ and} \tag{14}$$

$$E^{\mathrm{MOF}}(\boldsymbol{n}, d) = \left\|\boldsymbol{x}^{\mathrm{ref}}_{\mathrm{COM}} - \boldsymbol{x}^{\mathrm{act}}_{\mathrm{COM}}(\boldsymbol{n}, d)\right\|_2. \tag{15}$$

All the variables containing the superscript "ref" represents the variables pertaining to the original (*reference*) interface while those containing the superscript "act" represents the variables pertaining to the reconstructed (*actual*)

interface. For the purpose of illustration, Figure 1 shows a typical computational cell in 2D with the reference (solid curved line) and PLIC reconstructed (dashed straight line) interfaces based on liquid as reference fluid.

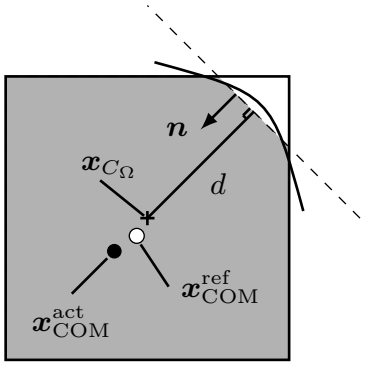

Figure 1: Computational cell with reference (solid curved line) and reconstructed (dashed straight line) interfaces and liquid centroid.

Within the context of numerical simulation of atomizing flows, the reference phase centroid corresponds to the centroid of the corresponding phase after advection of phase volume fraction in the domain. For example, the reference liquid centroid $\boldsymbol{x}^{\text{ref,liq}}_{\text{COM}}$ refers to the liquid phase centroid in a computational cell computed after the advection of liquid volume fraction field.

3.2.2. Solution Algorithm

In contrast to the works of Dyadechko and Shashkov [20] and Ahn and Shashkov [19], our work focuses mainly on the two-phase flows (the word "material" will be dropped hereon and will be referred as "phases"). This deems unnecessary for us to determine the best reconstruction order. Instead, following the proposition by Jemison et al. [23], we reconstruct the interface by choosing a reference phase with its *reference* centroid farthest from computational cell center, i.e.,

$$\text{Reference phase} = \begin{cases} \text{liquid}, & \left\| \boldsymbol{x}^{\text{liq}}_{\text{COM}} - \boldsymbol{x}_{C_\Omega} \right\|_2 > \| \boldsymbol{x}^{\text{gas}}_{\text{COM}} - \boldsymbol{x}_{C_\Omega} \|_2 \\ \text{gas}, & \text{otherwise.} \end{cases} \tag{16}$$

In other words, the centroid defect is minimized for the phase with the least volume in the cell. An illustration in 2D for choosing the reference fluid phase is shown in Figure 2. The rationale behind this approach is that, a

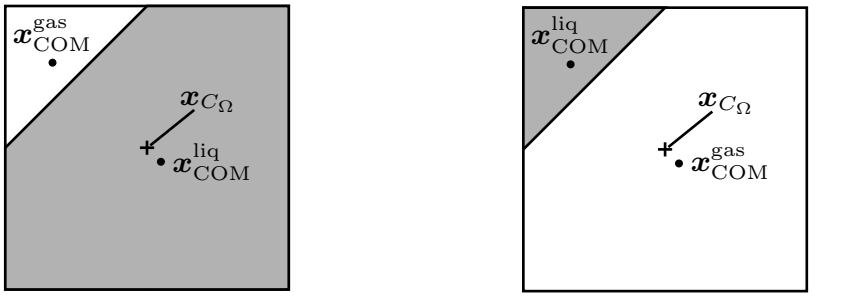

(a) Reference phase = gas (b) Reference phase = liquid

Figure 2: Determining reference fluid phase based on phase centroid–cell center distance.

small modification in the position of the centroid of the phase with largest volume has a high impact on the orientation of the interface. This is because a small error in the location of the $\boldsymbol{x}^{\text{act}}$ arising from the interface reconstruction (performed using this phase) will put the phase with least volume at the wrong location in the cell, consequently changing the orientation of the interface. Thus, it is imperative to reconstruct the interface using the phase with least volume to have the least error in interface reconstruction.

Once the reference fluid is chosen, the Equations (14) and (15) are solved respectively for d and $\boldsymbol{n}$ according to the following algorithms.

Step 1: determine interface–cell center distance d

The parameter d is related to the shortest distance between the interface plane and the computational cell center. It is computed as a result of satisfying the volume conservation condition (Equation (14)) upto the machine precision. We have implemented the geometric method of Gueyffier et al. [35] to compute the parameter d.

Step 2: determine interface unit normal $\boldsymbol{n}$

The computation of optimal interface unit normal $\boldsymbol{n}$ is obtained as a result of the minimization of the centroid defect E^{MOF} in Equation (15). Multiple methods exist for the minimization of this defect. In this work, we adopt the method explained by Jemison et al. [23] for the computation of interface unit normal. The minimization problem reads: find $\boldsymbol{n}$ such that E^{MOF} is minimum. To this end, we first parameterize the unit normal in spherical

coordinates as

$$\boldsymbol{n} = \begin{bmatrix} a \\ b \\ c \end{bmatrix} = \begin{bmatrix} \sin\Phi\cos\Theta \\ \sin\Phi\sin\Theta \\ \cos\Phi \end{bmatrix}. \tag{17}$$

We therefore simplified the resolution of the least square problem. Thus, the new problem statement reads: find the optimal values $(\Phi^{\text{opt}}, \Theta^{\text{opt}})$ such that $E^{\text{MOF}}(\Phi, \Theta, d) = g(\Phi, \Theta, d)$ is minimum. This can be framed mathematically as

$$E^{\text{MOF}}_{\text{min}}(\Phi^{\text{opt}}, \Theta^{\text{opt}}, d) = \min(E^{\text{MOF}}(\Phi, \Theta, d)) = \min_{\forall(\Phi,\Theta):\text{Eq.}(14)\text{ holds}} \|\boldsymbol{g}(\Phi, \Theta, d)\|_2 , \tag{18}$$

where $\boldsymbol{g}(\Phi, \Theta, d) = \boldsymbol{x}^{\text{ref}}_{\text{COM}} - \boldsymbol{x}^{\text{act}}_{\text{COM}}(\Phi, \Theta, d)$ with $\boldsymbol{g} : \mathbb{R}^3 \to \mathbb{R}^2$. This equation is solved as a non-linear least square problem using Gauss-Newton minimization algorithm [36, 37]. This algorithm is a superset of the Newton-Raphson method, thus, the initial guess has a significant impact in the convergence to the minima. To that end, we compute the initial guess for the normal from level set function ϕ as

$$\boldsymbol{N}^0 = \frac{1}{2\Delta x} \begin{bmatrix} \phi_{i+1,j,k} - \phi_{i-1,j,k} \\ \phi_{i,j+1,k} - \phi_{i,j-1,k} \\ \phi_{i,j,k+1} - \phi_{i,j,k-1}. \end{bmatrix} \tag{19}$$

This is then normalized

$$\boldsymbol{n}^0 = \frac{\boldsymbol{N}^0}{\|\boldsymbol{N}^0\|_2} \tag{20}$$

to obtain the initial guess for the unit normal $\boldsymbol{n}^0$. It is straightforward to retrieve the initial guess for the normal angles (Φ^0, Θ^0) using the relation given in Equation (17). Since our solver uses equidistant structured Cartesian mesh, it becomes relatively easier to compute the initial guess for the interface unit normal from the level set function. Algorithm 1 gives a pseudocode of the steps involved in Gauss-Newton minimization algorithm implemented in our solver. This algorithm is repeated for each mixed computational cell for each time step in the solution procedure. The partial derivatives in the computation of Jacobian matrix $\boldsymbol{J}$ are determined using central difference scheme as follows

$$\frac{\partial \boldsymbol{g}}{\partial \Phi} = \frac{\boldsymbol{g}(\Phi + \epsilon, \Theta) - \boldsymbol{g}(\Phi - \epsilon, \Theta)}{2\epsilon}, \tag{21}$$

$$\frac{\partial \boldsymbol{g}}{\partial \Theta} = \frac{\boldsymbol{g}(\Phi, \Theta + \epsilon) - \boldsymbol{g}(\Phi, \Theta - \epsilon)}{2\epsilon}, \tag{22}$$

Algorithm 1 Gauss-Newton minimization algorithm

function GAUSSNEWTON_MOF($a^0, b^0, c^0, d^0, \Phi^0, \Theta^0, F^{\text{ref}}, \boldsymbol{x}^{\text{ref}}_{\text{COM}}$)
  ctr $= 1$
  tolg $= 1E-08$
  tolJ $= 1E-13$
  loop
    $d^{\text{ctr}} \leftarrow\mid F^{\text{ref}} - F^{\text{act}}(\boldsymbol{n}^{\text{ctr}-1}, d) \mid = 0$ ▷ Section 3.2.2
    $\mid \omega^{\text{ctr}} \mid\leftarrow a^{\text{ctr}-1}, b^{\text{ctr}-1}, c^{\text{ctr}-1}, d^{\text{ctr}}$
    $\boldsymbol{x}^{\text{act,ctr}}_{\text{COM}} \leftarrow (a^{\text{ctr}-1}, b^{\text{ctr}-1}, c^{\text{ctr}-1}, d^{\text{ctr}}, F^{\text{ref}})$ ▷ Equation (13)
    $\boldsymbol{g}^{\text{ctr}}(\Phi^{\text{ctr}-1}, \Theta^{\text{ctr}-1}, d^{\text{ctr}}) = \boldsymbol{x}^{\text{ref}}_{\text{COM}} - \boldsymbol{x}^{\text{act,ctr}}_{\text{COM}}$
    $\boldsymbol{J}^{\text{ctr}}(\boldsymbol{g}) = \left[\frac{\partial \boldsymbol{g}^{\text{ctr}}}{\partial \Phi} \frac{\partial \boldsymbol{g}^{\text{ctr}}}{\partial \Theta}\right]$ ▷ Jacobian matrix
    $Q = \left\| \left(\boldsymbol{J}^{\text{ctr}}\right)^T \cdot \boldsymbol{g} \right\|_2$
    if $((Q \leq \texttt{tolJ})$ .or. $(\|\boldsymbol{g}^{\text{ctr}}\|_2 < \texttt{tolg}))$ **then**
      exit
    else if $(\text{ctr} == 20)$ **then**
      exit
    else
      $(\Phi^{\{\text{ctr}+1\}}, \Theta^{\{\text{ctr}+1\}}) = (\Phi^{\text{ctr}}, \Theta^{\text{ctr}}) + \left(\left(\boldsymbol{J}^{\text{ctr}}_g\right)^T \boldsymbol{J}^{\text{ctr}}_g\right)^{-1} \left(\boldsymbol{J}^{\text{ctr}}_g\right)^T \boldsymbol{g}^{\text{ctr}}$
      ctr $=$ ctr $+ 1$
    end if
  end loop
  $\boldsymbol{x}^{\text{ref}}_{\text{COM}} \leftarrow \boldsymbol{x}^{\text{act,ctr}}_{\text{COM}}$
  return (Φ, Θ)
end function

with the $\epsilon = \pi/10\,000$. It is to be mentioned that this minimization algorithm finds local minima and not the global minima. Nevertheless, it is the best approximation we can obtain with relatively less computational cost. Finally, the pseudocode of the overall procedure of our MOF interface reconstruction method implemented in our solver is summarized in Algorithm 2. In this algorithm, the value of ξ has been chosen to be 1×10^{-12}.

3.3. Phase moments transport

In order to perform high fidelity numerical simulation of multiphase flows, it is imperative that the phase-based quantities are transported accurately. Within the context of MOF method, *reference* liquid volume fraction F^{ref} and

Algorithm 2 MOF Interface Reconstruction algorithm

procedure MOF_RECONSTRUCTION
  for it = 1, nt **do** ▷ time loop
    for k = kmin-1, kmax+1 **do**
      for j = jmin-1, jmax+1 **do**
        for i = imin-1, imax+1 **do**
          if $((F^{\text{ref}} \leq \xi)$ .or. $(F^{\text{ref}} \geq 1-\xi))$ **then** ▷ Empty/full cell
            $a, b, c = 0$
            $d = 4 \times (F^{\text{ref}} - 0.5) \times \Delta x$
            $\boldsymbol{x}^{\text{ref}}_{\text{COM,liq}} = 0.5 \times F^{\text{ref}}$
            $\boldsymbol{x}^{\text{ref}}_{\text{COM,gas}} = 0.5 \times (1 - F^{\text{ref}})$
            cycle
          else ▷ Mixed cell
            $l_{\text{ccl}} = \left\| \boldsymbol{x}^{\text{ref,liq}}_{\text{COM}} - \boldsymbol{x}_{C_\Omega} \right\|_2$
            $l_{\text{ccg}} = \left\| \boldsymbol{x}^{\text{ref,gas}}_{\text{COM}} - \boldsymbol{x}_{C_\Omega} \right\|_2$
            $\boldsymbol{n}^{\text{it}-1} \leftarrow \phi$
            $[a^{\text{it}-1}, b^{\text{it}-1}, c^{\text{it}-1}]^T \leftarrow \boldsymbol{n}^{\text{it}-1}$ ▷ Equation (17)
            if $(l_{\text{ccl}} > l_{\text{ccg}})$ **then** ▷ Ref phase = liquid
              $(\Phi^{\text{it}-1}, \Theta^{\text{it}-1}) \leftarrow [a^{\text{it}-1}, b^{\text{it}-1}, c^{\text{it}-1}]^T$
              $(\Phi, \Theta) = \text{GaussNewton\_MOF}(a^0, b^0, c^0, d^0, \Phi^0, \Theta^0, F^{\text{ref}}, \boldsymbol{x}^{\text{ref,liq}}_{\text{COM}})$
              $(a, b, c) \leftarrow (\Phi, \Theta)$
            else ▷ Ref phase = gas
              $(\Phi^{\text{it}-1}, \Theta^{\text{it}-1}) \leftarrow [-a^{\text{it}-1}, -b^{\text{it}-1}, -c^{\text{it}-1}]^T$
              $F^{\text{ref,gas}} = 1 - F^{\text{ref}}$
              $(\Phi, \Theta) = \text{GaussNewton\_MOF}(a^0, b^0, c^0, d^0, \Phi^0, \Theta^0, F^{\text{ref,gas}}, \boldsymbol{x}^{\text{ref,gas}}_{\text{COM}})$
              $(-a, -b, -c) \leftarrow (\Phi, \Theta)$
            end if
            $\boldsymbol{n} = [a, b, c]^T$
            $|\ \omega\ | \leftarrow a, b, c, d$
          end if
        end for
      end for
    end for
  end for
  return $a, b, c, d, \boldsymbol{x}^{\text{ref,liq}}_{\text{COM}}, \boldsymbol{x}^{\text{ref,gas}}_{\text{COM}}$
end procedure

reference centroids of liquid $\boldsymbol{x}^{\text{ref}}_{\text{COM,liq}}$ and gas $\boldsymbol{x}^{\text{ref}}_{\text{COM,gas}}$ phases are transported simultaneously in each Cartesian direction. Hence, the superscript "ref" is dropped for the remainder of this section, since the quantities pertain only to the reference interface. It is important that this advection is performed consistently with that of the liquid volume fraction.

3.3.1. Phase centroid transport

The numerical method behind advection of reference phase centroids is now presented. In our work, we have used phase centroid as an *approximated* Lagrangian particle that is associated to its phase packet [20]. Accordingly, a simple *approximated* Lagrangian equation (see [20, Appendix A] for derivation) is used for the advection of reference phase centroid $\boldsymbol{x}^{\text{ref}}_{\text{COM}}$ which is given as

$$\frac{\partial \boldsymbol{x}_{\text{COM}}}{\partial t} = \boldsymbol{u}(\boldsymbol{x}_{\text{COM}}). \tag{23}$$

In Equation (23), the face-centered velocity components in each computational cell are linearly interpolated to the location of the centroid to obtain $\boldsymbol{u}(\boldsymbol{x}_{\text{COM}})$. It is to be remarked that phase centroids for liquid and gas phase are stored for a mapped unit computational cell, hence, their value is always in the range $[0, 1]$. During the advection step, each phase centroid coordinate is remapped back to the physical computational cell. Such a mapping–remapping procedure is carried out to ease out the interface reconstruction procedure. A directionally split advection algorithm with Eulerian Implicit–Lagrangian Explicit (EI–LE) scheme is used for the advection. A simple first-order time integration of this equation keeping constant velocity over the time step size Δt yields,

$$\boldsymbol{x}^{n+1}_{\text{COM}} = \boldsymbol{x}^{n}_{\text{COM}} + \boldsymbol{u}(\boldsymbol{x}^{*}_{\text{COM}})\Delta t. \tag{24}$$

The mode of the scheme is Eulerian Implicit if $\boldsymbol{x}^{*}_{\text{COM}} = \boldsymbol{x}^{n+1}_{\text{COM}}$ and Lagrangian Explicit if $\boldsymbol{x}^{*}_{\text{COM}} = \boldsymbol{x}^{n}_{\text{COM}}$. Consider a 2D computational cell $C_{\Omega_{i,j}} = [x_{i-1/2}, x_{i+1/2}] \times [y_{j-1/2}, y_{j+1/2}]$ with the face-centered velocity components given as $u_{i+1/2,j}$, $u_{i-1/2,j}$, $v_{i,j+1/2}$, and $v_{i,j-1/2}$. Let the liquid phase centroid be located at $(x_{\text{COM}}, y_{\text{COM}})$. Without loss of generality, the interpolation along $x-$direction is presented as follows. The implementation of the interpolation along $y-$direction (and $z-$direction in 3D) are alike.

$$u(x^{*}_{\text{COM}}) = u_{i-1/2,j}(x_{i+1/2} - x^{*}_{\text{COM}}) + u_{i+1/2,j}(x^{*}_{\text{COM}} - x_{i-1/2}) \tag{25}$$

In the case of Eulerian Implicit (EI) scheme where $x^*_{\text{COM}} = x^{n+1}_{\text{COM}}$, Equation (24) transforms to

$$x^{n+1}_{\text{COM}} = E(x^n_{\text{COM}} - (u_{i+1/2,j}x_{i-1/2} - u_{i-1/2,j}x_{i+1/2})) \tag{26}$$

with $E = 1/(1 - (u_{i+1/2,j} - u_{i-1/2,j}))$ whereas in the case of Lagrangian Explicit scheme with $x^*_{\text{COM}} = x^n_{\text{COM}}$, the Equation (24) becomes

$$x^{n+1}_{\text{COM}} = Lx^n_{\text{COM}} - (u_{i+1/2,j}x_{i-1/2} - u_{i-1/2,j}x_{i+1/2}) \tag{27}$$

with $L = 1 + u_{i+1/2,j} - u_{i-1/2,j}$. By changing the order of this scheme for the advection directions between adjacent time steps ensures a consistent advection of the phase centroids with their phase packet volume in the domain. A more clear picture of this switching of the schemes is given in Equation (28).

$$\begin{aligned} t^n \rightarrow t^{n+1} &: x(\text{EI}) - y(\text{LE}) - z(\text{EI}), \\ t^{n+1} \rightarrow t^{n+2} &: y(\text{EI}) - z(\text{LE}) - x(\text{LE}), \\ t^{n+2} \rightarrow t^{n+3} &: z(\text{EI}) - x(\text{EI}) - y(\text{LE}), \\ &\text{repeat.} \end{aligned} \tag{28}$$

3.3.2. Advection procedure

To give a better visualization of the advection steps, let us consider a simple 3-stencil computational cell layout with liquid (dark region) as shown in Figure 3. For the sake of simplicity, let us consider the direction of velocity (with the other components of velocity equal to zero) as shown in this figure. The new liquid that will be entering the cell i from $i-1$ and with the displacement of the existing liquid within cell i would change the the coordinates of the phase centroids in cell i. Let the domain of the cell i be given as $C_{\Omega_i} = [x_{i-1/2}, x_{i+1/2}] \times [y_{j-1/2}, y_{j+1/2}]$. The objective is to find the new phase centroids of the cell i after advection.

Without loss of generality, the advection of liquid reference centroid along $x-$direction is chosen for presentation. The advection along $y-$ and $z-$directions are carried out alike. The advection for the gas phase counterpart is performed identically and its implementation is straightforward. It is to be remarked that the interface reconstruction is carried out before its advection. Thus, we have the information about the unit normal coefficients and the liquid volume fraction in each computation cell *apriori*. The advection procedure goes as follows and is illustrated in Figure 4:

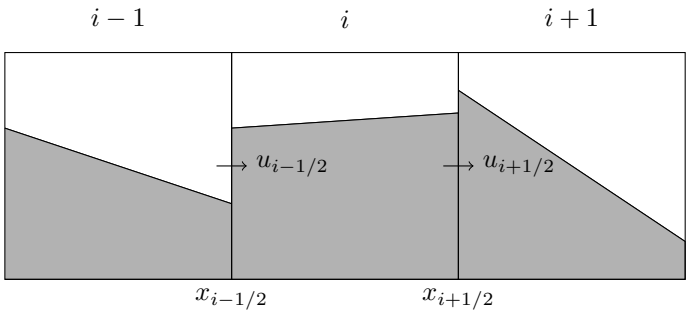

Figure 3: 3-cell stencil for advection of liquid centroid. Liquid depicted as dark fluid.

(a) Find the domain and volume of the region of liquid that will be entering or moving to cell i called hereon as departure region corresponding to the dashed outlined region in Figure 4a. Thus,

$$C_{\Omega_{i_{\text{depart}}}} = [x_{i-1/2} - u_{i-1/2}\Delta t, x_{i+1/2} - u_{i+1/2}\Delta t] \times [y_{j-1/2}, y_{j+1/2}]. \quad (29)$$

(b) Find the domain and volume of individual regions of liquid entering or displacing each from cell $i-1$ (dashed outlined region) and i (dot dashed outlined region) called hereon as intersected departure regions (c.f. Figure 4b). Therefore, we have

$$C_{\Omega_{i',i}} = C_{\Omega_{i+i'}} \cap C_{\Omega_{i_{\text{depart}}}} \forall i' = -1, 0, 1. \quad (30)$$

(c) Compute the liquid phase centroid of each of these interesected departure region (c.f. Figure 4c) using Equation (13).

(d) Advect this centroid using EI–LE scheme according to Equation (23) (c.f. Figure 4d).

(e) Compute the new liquid phase centroid for cell i as weighted average of all the centroids of liquid phase packets entering or displaced within cell i with volume of each liquid packet. This is given as

$$\boldsymbol{x}^{n+1}_{\text{COM}_i} = \frac{\sum_{i'=-1}^{1} \boldsymbol{x}_{\text{COM}_{\Omega_{i,i'}}} \mid C_{\Omega_{i',i}} \mid}{\sum_{i'=-1}^{1} \mid C_{\Omega_{i',i}} \mid}, \quad (31)$$

where $\mid C_{\Omega_{i',i}} \mid$ represent the liquid volume of the corresponding intersected departure region.

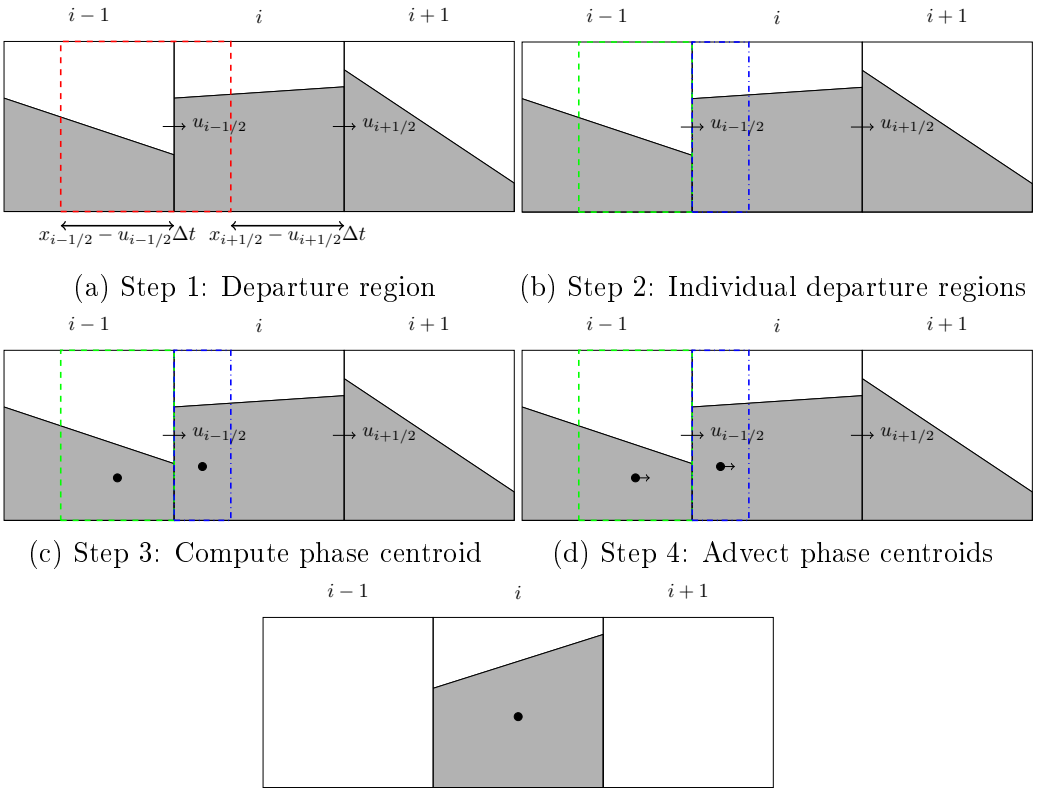

(a) Step 1: Departure region

(b) Step 2: Individual departure regions

(c) Step 3: Compute phase centroid

(d) Step 4: Advect phase centroids

(e) Step 5: Weighted averaged centroid

Figure 4: Step-by-step procedure of advection of liquid phase centroid.

4. Verification tests and numerical results

With the presentation of the MOF method, we now present the results from transport and deformation tests for verifying and assessing the accuracy of the liquid/gas interface reconstruction. Each of these tests are time reversible T-periodic tests. The accuracy of the interface reconstruction is measured based on two error norms. They are as follows:

- Symmetric error: This error, proposed by Dyadechko and Shashkov [20], measures the area between the two interfaces giving a measure of the accuracy in the orientation of the interface normal in addition to the amount of liquid volume it encompasses under the interface. It is shown as dark region in Figure 5. The computation of this error can

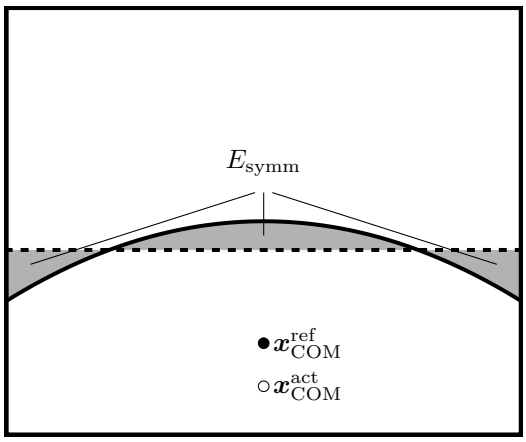

Figure 5: Illustration of symmetric difference area error shown as grey regions along with reference interface (solid line) and actual/reconstructed interface (dashed line).

be mathematically expressed as

$$E_{\text{symm}} = \mid \omega^{\text{ref}} \cup \omega^{\text{act}} - \omega^{\text{ref}} \cap \omega^{\text{act}} \mid \tag{32}$$

This expression can be simplified in terms of the Heaviside function as

$$E_{\text{symm}} = \sum_{i,j,k} \int_{C_{\Omega_{i,j,k}}} \Big| H(\boldsymbol{n} \cdot (\boldsymbol{x} - \boldsymbol{x}_{\boldsymbol{C_\Omega}}) + d) - H(\phi_{\text{exact}}(\boldsymbol{x})) \Big| d\boldsymbol{x}, \tag{33}$$

where ϕ_{exact} is the level set function of the exact interface determined analytically. It is to be remarked that this error is measured after the interface comes back to its initial position, i.e., $t = T$. The integral in this expression is evaluated using quadrature method by dividing each computational cell $C_{\Omega_{i,j,k}}$ into 128 subcells in each coordinate direction.

- Geometric error: this error measures the discrepancy between the reference and reconstructed interfaces in terms of shape of the object. Similar to the symmetric difference error, this error estimate is also computed at the final instant when the interface comes back to its initial position. This error metric is expressed as

$$E_{\text{geo}} = \int_{\Omega} \Big| F(\boldsymbol{x}, T) - F(\boldsymbol{x}, 0) \Big| d\boldsymbol{x}. \tag{34}$$

4.1. Zalesak's disk

First, we present the rigid body rotation of a notched circular disk (Zalesak's disk) of liquid that were performed in many studies, for example [18, 38, 39]. This test assess the capability of MOF method to accurately transport the sharp corners. To this end, a circular disk of radius 0.15 with a slot width of 0.06 and slot length of 0.2 placed at $(0.5, 0.75)$ in a $[0, 1] \times [0, 1]$ domain is rotated about the domain center using the following velocity field

$$u = \frac{\pi}{3.14}(0.5 - y), \quad \text{and} \tag{35}$$

$$v = \frac{\pi}{3.14}(x - 0.5). \tag{36}$$

The test concludes when the disk completes one full rotation in the domain. For the considered size of the domain, the time at which the disk completed one full rotation is at $t = T = 2\pi$. Multiple mesh resolutions ranging from 32×32 to 1024×1024 were used for the discretization of the domain. The time integration has been performed using forward Euler scheme with a CFL of 0.5.

The interface shapes after one full rotation are shown in Figure 6 for MOF and CLSVOF methods for three mesh resolutions. The black solid line represents the initial interface and the red dashed line represents the final interface of the disk after one full rotation. The interface contours are represented as the zero-level isocontour of the level set function in our solver. It can be clearly seen that the MOF method is able to well capture the sharp corners of the disk. These sharp corners are the regions of high curvature concentration in the interface shape. In fact, these corners are better captured when using MOF method than using CLSVOF method. Furthermore, as the mesh resolution increases, the final shape of the interface tends towards the initial shape.

A quantitative analysis of the error estimates are shown in Figure 7 for both MOF (filled black circles) and CLSVOF (filled red triangles) methods. The first and second-order error convergence lines are also shown in these plots as dashed and dash dotted lines respectively. From these plots, we find that both the symmetric difference area error and geometric error estimates displays second-order convergence. Furthermore, we find that MOF method is displaying less error estimate than CLSVOF method for all the mesh resolutions under consideration. Finally, Table 1 summarizes the error estimates for the MOF and CLSVOF methods for various mesh resolutions with the

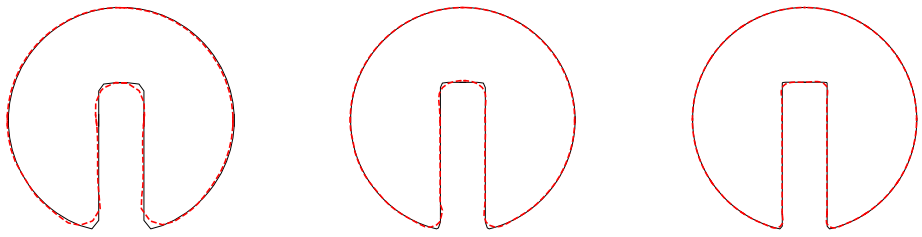

(a) MOF: 64×64 (b) MOF: 128×128 (c) MOF: 256×256

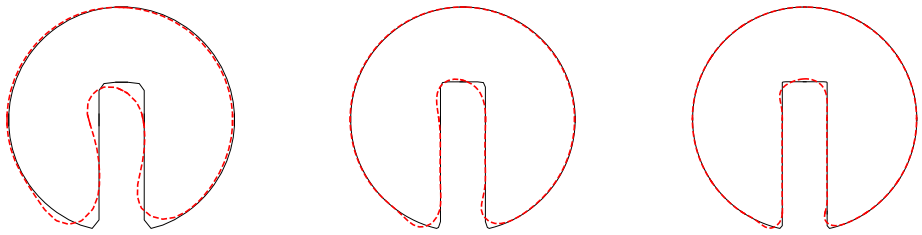

(d) CLSVOF: 64×64 (e) CLSVOF: 128×128 (f) CLSVOF: 256×256

Figure 6: Comparison of results from one rotation of Zalesak's disk using MOF ((a), (b), (c)) and CLSVOF ((d), (e), (f)) methods for multiple mesh resolutions: initial interface (——), final interface (- - -).

error convergence order given within the parantheses for each column of the error estimate.

Table 1: Summary of error estimates for Zalesak's disk test with spatial order of error convergence given within parantheses.

N_x	MOF		CLSVOF	
	E_{symm}	E_{geo}	E_{symm}	E_{geo}
32	3.95E-04	1.18E-04	1.65E-03	6.15E-04
64	5.99E-05 (2.72)	1.95E-05 (2.60)	2.96E-04 (2.48)	1.13E-04 (2.44)
128	1.53E-05 (1.97)	6.19E-06 (1.66)	8.31E-05 (1.83)	2.52E-05 (2.17)
256	3.21E-06 (2.25)	1.27E-06 (2.29)	2.20E-05 (1.92)	7.32E-06 (1.78)
512	7.42E-07 (2.11)	2.70E-07 (2.23)	5.22E-06 (2.08)	1.41E-06 (2.38)
1024	1.58E-07 (2.23)	6.01E-08 (2.17)	1.39E-06 (1.91)	4.61E-07 (1.61)

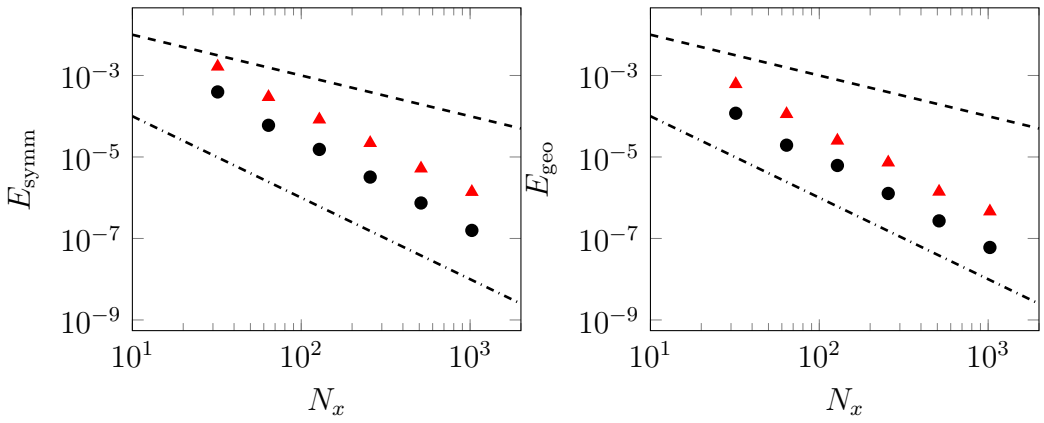

(a) Symmetric difference area error (b) Geometric error

Figure 7: Error estimates for Zalesak's disk rotation test: MOF (●); CLSVOF (▲); first-order convergence line (- - -); second-order convergence line (-·-·-).

4.2. Circle in a deformation field

The test for the deformation of a circular fluid body by a single vortex under solenoidal velocity field is considered as a benchmark test to assess the ability of the numerical method of interface reconstruction to capture thin filaments [13, 17]. In this test, the a circle of radius 0.15 with its center located at $(0.5, 0.75)$ in a $[0,1]\times[0,1]$ domain is made to undergo deformation under the given solenoidal field

$$u = -2\sin^2(\pi x)\sin(\pi y)\cos(\pi y)\cos(\pi t/T) \tag{37}$$

$$v = 2\sin^2(\pi y)\sin(\pi x)\cos(\pi x)\cos(\pi t/T) \tag{38}$$

where the time period of the test $T = 8$. This velocity field stretches and tears the initially circular fluid body as it becomes progressively entrained by the vortex reaching maximum deformation at $T/2$ and comes back to its original shape at time $t = T$. The entrainment is demonstrated as long thin fluid filament spiraling inward towards the vortex center. Five different mesh resolutions ranging from 32×32 to 1024×1024 are considered for this verification test. The CFL was maintained constant to a value of 0.5 throughout the test for all mesh resolutions.

Figures 8 and 9 shows the phase interface at $t = T/2$ and T for MOF and CLSVOF methods for 64×64, 128×128, and 256×256 mesh resolutions. The solution computed on 512×512 grid does not have any visual difference

from that computed on 256×256 grid. The reference solution (depicted by black solid line in the subfigures) is obtained on a 1024×1024 grid using MOF and CLSVOF method respectively for Figure 8 and Figure 9. Clearly, the MOF method is proving to be a better method in capturing the thin filaments of the stretched circle for a mesh resolution of 128×128.

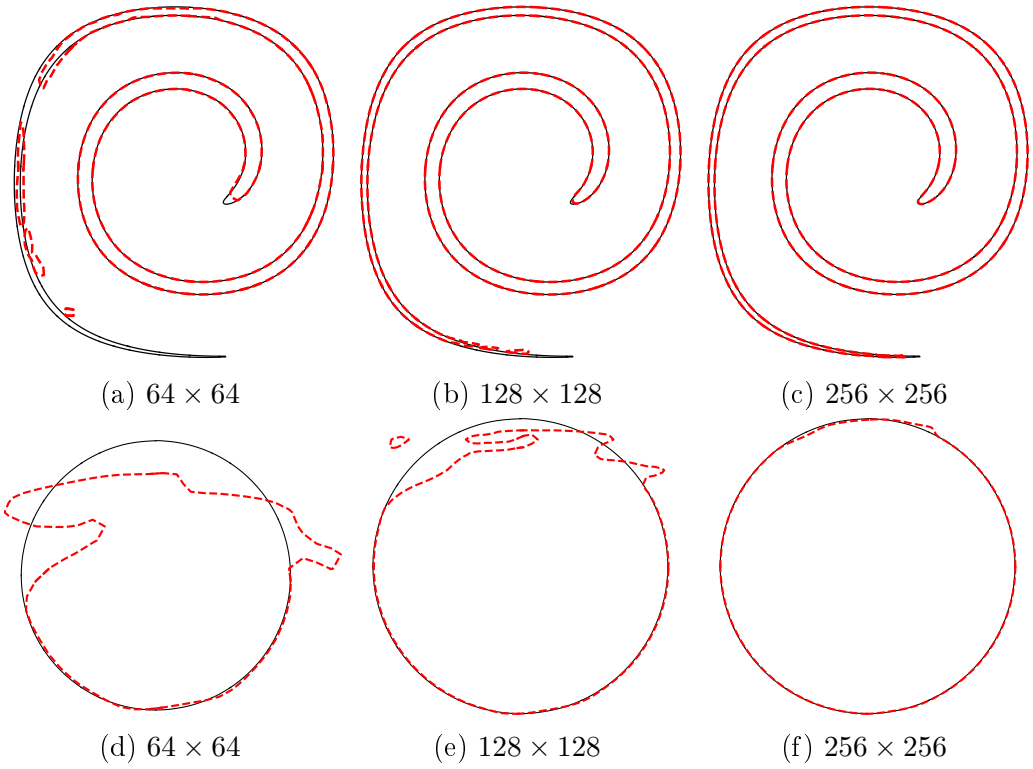

(a) 64×64 (b) 128×128 (c) 256×256

(d) 64×64 (e) 128×128 (f) 256×256

Figure 8: Phase interface shape for circle deformation test using MOF method for 64×64, 128×128, and 256×256 mesh resolutions: reference solution (——), computed interface (- - -).

The error estimates for this test are shown in Figure 10 for all the five mesh resolutions considered for this test. The CFL number was maintained constant to a value of 0.5 throughout the simulation for all the mesh resolutions. It can be seen clearly that the symmetric difference area is demonstrating a first-order convergence with the CLSVOF method showing the same order of error as that of MOF for higher mesh resolutions. This is in striking contrast to the result observed for Zalesak's disk test in which MOF method consistently showed lower error estimate than CLSVOF method. This is be-

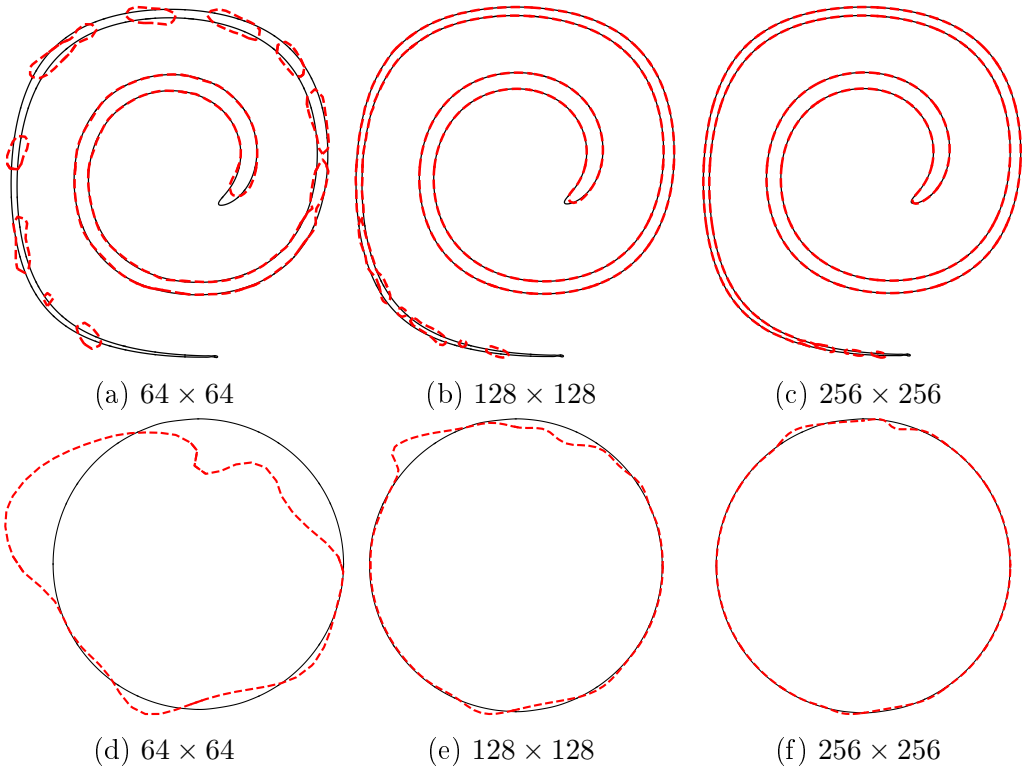

(a) 64×64 (b) 128×128 (c) 256×256

(d) 64×64 (e) 128×128 (f) 256×256

Figure 9: Phase interface shape for circle deformation test using CLSVOF method for 64×64, 128×128, and 256×256 mesh resolutions: reference solution (——), computed interface (- - -).

cause the sharp corners of the Zalesak's disk can cause inaccurate orientation of interface unit normal resulting in higher symmetric difference area for the CLSVOF. Therefore, increasing the mesh resolution better captures the corners resulting in faster decrease in error and higher error convergence order. On the other hand, this test deals with smooth circle deformation leading to under-resolved filament at its ends under maximum deformation. Increasing the mesh resolution will still be capturing the same overall interface shape but with better capture of these filaments. Hence, the symmetric difference area error estimate decreases slowly with increasing mesh resolution leading to first-order convergence. Although the geometric error shows second-order convergence, it is also experiencing the same trend as that of the symmetric difference area error with respect to the order of magnitude of error for MOF and CLSVOF methods. It is observed that the CLSVOF methods

are demonstrating a comparable error estimate as that of the MOF method but the latter method is able to well capture the tail of the deformed circle without artificial breakup as shown in Figure 8c. Finally, the error estimate

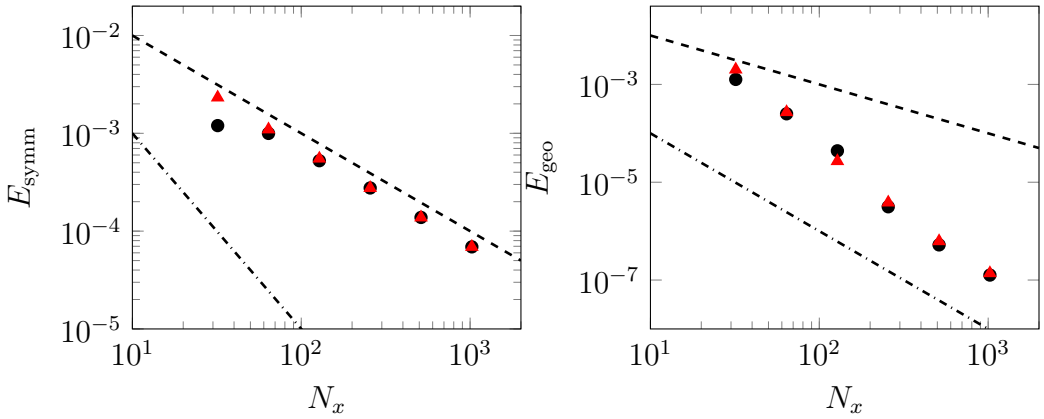

(a) Symmetric difference area error (b) Geometric error

Figure 10: Error estimates for circle deformation test: MOF (●); CLSVOF (▲); first-order convergence line (- - -); second-order convergence line (-·-·-).

values are summarized in Table 2 along with their order of convergence with increasing spatial mesh resolution. The symmetric difference area error reported in this table are consistently of lower order and value in comparison to those reported by Jemison et al. [23]. Their value of errors are reported by using a one-level adaptive mesh refinement (AMR).

Table 2: Summary of error estimates for circle deformation test with spatial order of error convergence given within parantheses.

N_x	MOF		CLSVOF	
	E_{symm}	E_{geo}	E_{symm}	E_{geo}
32	1.20E-03	1.27E-03	2.32E-03	2.02E-03
64	9.97E-04 (0.27)	2.51E-04 (2.34)	1.10E-03 (1.08)	2.71E-04 (2.90)
128	5.25E-04 (0.93)	4.39E-05 (2.52)	5.52E-04 (0.99)	2.70E-05 (3.33)
256	2.76E-04 (0.93)	3.15E-06 (3.80)	2.76E-04 (1.00)	3.85E-06 (2.81)
512	1.38E-04 (1.00)	5.23E-07 (2.59)	1.38E-04 (1.00)	6.22E-07 (2.63)
1024	6.90E-05 (1.00)	1.26E-07 (2.05)	6.90E-05 (1.00)	1.38E-07 (2.17)

4.3. Sphere in a deformation field

In the previous test, a non-linear velocity field is applied to a two dimensional circular liquid body. Often in multiphase flows, the complex topological structures are in three dimensions. Thus, to test the accuracy of the numerical method, we now apply a non-linear time reversing solenoidal velocity field on a spherical liquid droplet. This test was first proposed by Enright et al. [40] using a velocity field presented in the work of LeVeque [41]. The velocity field is given by

$$u(x,y,z,t) = 2\sin^2(\pi x)\sin(2\pi y)\sin(2\pi z)\cos(\pi t/3) \tag{39}$$

$$v(x,y,z,t) = -\sin(2\pi x)\sin^2(\pi y)\sin(2\pi z)\cos(\pi t/3) \tag{40}$$

$$w(x,y,z,t) = -\sin(2\pi x)\sin(2\pi y)\sin^2(\pi z)\cos(\pi t/3) \tag{41}$$

where x, y, z are spatial coordinates and t is the simulation time. In this test, a spherical liquid droplet of radius 0.15 placed with its center located at $(0.35, 0.35, 0.35)$ inside a $[0,1]\times[0,1]\times[0,1]$ domain. With this time reversing velocity field, an initial spherical interface is stretched to form a thin sheet at $t = 1.5$ and reverses back to its original spherical shape at $t = T = 3$.

Figure 11 shows the phase interface represented using zero level of the level set function for the 192^3 mesh resolution using MOF and CLSVOF methods. It can be seen that although CLSVOF method is able to capture the thin sheet membrane of the stretched sphere, the final interface shape has relatively more deformation than that of the MOF method. This deficiency of the CLSVOF method is reduced by the proposed MOF method.

The mesh convergence of the symmetric difference error and geometric error are shown in Figure 12 for five mesh resolutions ranging from 32^3 to 512^3. A constant CFL of 0.5 was maintained throughout the simulation for all the mesh resolutions considered for this test. From these plots, we can observe at least first-order convergence in spatial resolution for symmetric difference and geometric error estimates. Moreover, we find that the error estimates using CLSVOF method converges to those using MOF method. This is due to the fact that higher the mesh resolution lesser are the under-resolved interfacial regions in the domain thereby the CLSVOF method is able to capture the phase interface with as high accuracy as MOF method. Finally, Table 3 summarizes the error estimate values for MOF and CLSVOF method for various mesh resolutions with the error convergence order given within the parantheses for each column of the error estimate. The symmetric

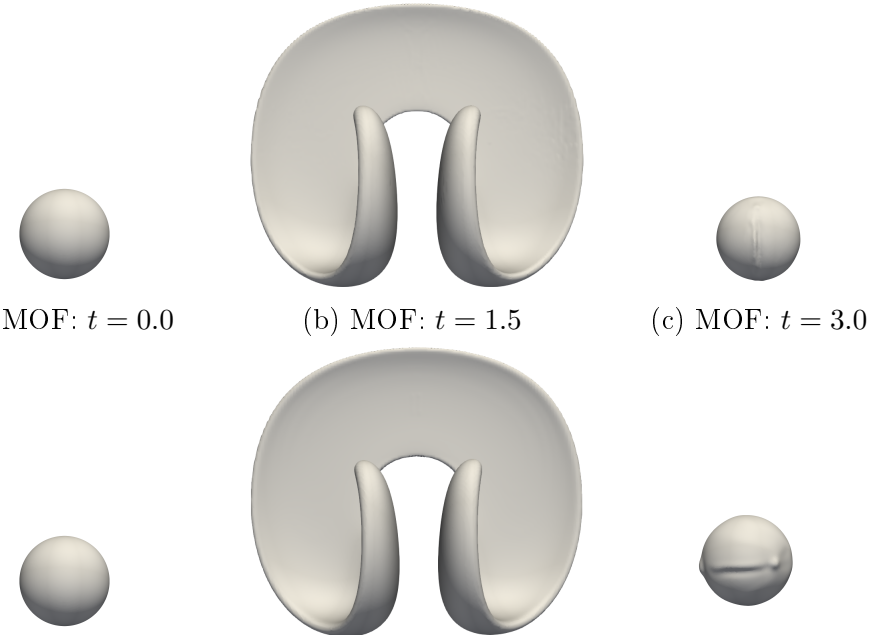

(a) MOF: $t = 0.0$ (b) MOF: $t = 1.5$ (c) MOF: $t = 3.0$

(d) CLSVOF: $t = 0.0$ (e) CLSVOF: $t = 1.5$ (f) CLSVOF: $t = 3.0$

Figure 11: Phase interface for 3D spherical droplet deformation for 192^3 mesh resolution using MOF and CLSVOF methods.

difference error estimates from our work are of the comparable order to that reported for this test by Jemison et al. [23].

Table 3: Summary of error estimates for sphere deformation test with spatial order of error convergence given within parantheses.

N_x	MOF		CLSVOF	
	E_{symm}	E_{geo}	E_{symm}	E_{geo}
32	6.83E-03	5.62E-03	8.52E-03	7.77E-03
64	2.99E-03 (1.19)	2.35E-03 (1.26)	3.78E-03 (1.17)	3.50E-03 (1.15)
128	8.38E-04 (1.84)	5.38E-04 (2.13)	9.47E-04 (1.99)	7.72E-04 (2.18)
192	3.91E-04 (1.88)	1.87E-04 (2.60)	4.64E-04 (1.83)	3.12E-04 (2.23)
256	3.14E-04 (1.42)	1.80E-04 (1.48)	3.39E-04 (1.50)	2.35E-04 (1.72)
512	1.43E-04 (1.14)	7.11E-05 (1.12)	1.56E-04 (1.12)	9.56E-05 (1.30)

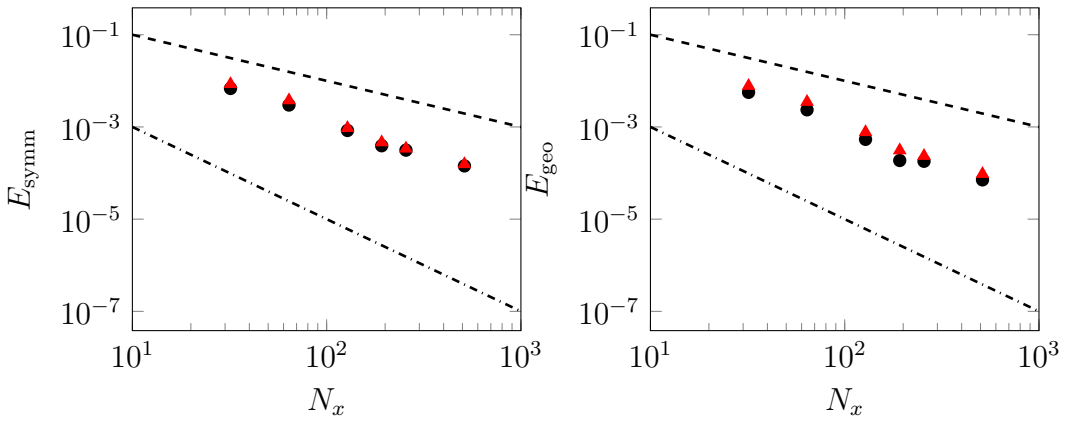

(a) Symmetric difference error (b) Geometric error

Figure 12: Error estimates for spherical droplet deformation test: MOF (●); CLSVOF (▲); first-order convergence line (- - -); second-order convergence line (-·-·-).

5. Solution to the Navier-Stokes equations

5.1. Flow solver

This subsection explains the coupling of the MOF method with our flow solver ARCHER [17, 32, 33] whose capabilities have been described extensively in multiple works [42, 43]. This solver is structured, parallel and developed for direct numerical simulations (DNS) of complex and turbulent multiphase flows with the application to study primary breakup of liquid fuel jet. This solver has been validated for various cases of complex turbulent flow configurations [44, 45] thus, the numerical methods employed in this solver are tailored for treating turbulence in the system.

A staggered grid configuration is used with central finite difference scheme for least numerical dissipation. The scalar variables such as liquid volume fraction, density, viscosity, level set function, and pressure are stored in the cell center while the vector variables such as components of velocity and vorticity are stored in cell faces. A second-order central difference scheme is employed for discretization of the spatial derivatives to avoid any dissipation. However, the convection term is discretized using fifth-order WENO scheme to ensure a robust behavior of the solution. Ghost Fluid Method (GFM) [46] is employed for the spatial discretization of the Poisson equation (Equation (45)) for taking into account the force due to surface tension as a pressure jump. The resulting linear system of symmetric and positive

definite matrix with five diagonals is solved using multigrid algorithm for preconditioning a conjugate gradient (CG) method [32].

5.2. Consistent mass and momentum flux computation

As mentioned by Rudman [47], it is necessary that the convective term in the Navier-Stokes Equation (2) is expressed in conservative form and to have consistency between the computation of mass and momentum flux. The Navier-Stokes equations in conservative form can be written as

$$\frac{\partial \rho}{\partial t} + \nabla \cdot (\rho \boldsymbol{u}) = 0 \tag{42}$$

$$\frac{\partial \rho \boldsymbol{u}}{\partial t} + \nabla \cdot (\rho \boldsymbol{u} \otimes \boldsymbol{u}) = -\boldsymbol{\nabla} P + \boldsymbol{\nabla} \cdot (2\mu \boldsymbol{D}) + \boldsymbol{B}. \tag{43}$$

In order to have consistent computation of mass and momentum flux, we use the method of Vaudor et al. [33] (based on the work of Rudman [47]) to efficiently compute the mass and momentum fluxes with a single-grid approach unlike dual-grid approach. Such a single grid approach reduces the computational cost significantly and achieves the same accuracy.

Although the mass conservation equation is not solved explicity in our solver, it is enforced by solving the advection equation of liquid volume fraction (c.f. Equation (11)). The mass flux is given as $\rho \boldsymbol{u}$ (deduced from liquid volume fraction flux) while the momentum flux is given as $\rho \boldsymbol{u} \otimes \boldsymbol{u}$. The problem of inconsistency between these fluxes arise due to the usage of staggered variable configuration. Such a configuration leads to two different control volumes for the density and velocity component. It is imperative that the computation of $\rho \boldsymbol{u}$ remains the same in both these equations. The method of Vaudor et al. [33] involves computation of pseudo fluxes on the faces of the intersected control volumes of density and velocity components thereby deducing the consistent computation of mass and momentum fluxes.

5.3. Projection Method

In order to solve the Equations (1) and (2), a projection method as described in Ménard et al. [17] is employed. The algorithm of implementation of this method in ARCHER is given below in brief:

Algorithm 3 Projection Method

1: Compute $\boldsymbol{u}^*$ (Predictor step):

$$\boldsymbol{u}^* = \frac{1}{\rho^{n+1}}\Big(\rho^n \boldsymbol{u}^n + \Delta t\Big(\nabla \cdot (\rho^n \boldsymbol{u}^n \boldsymbol{u}^n) + \nabla \cdot (2\mu^n \boldsymbol{D}) + \boldsymbol{B}\Big)\Big) \tag{44}$$

2: Solve for pressure P^{n+1} (Poisson equation for pressure):

$$\boldsymbol{\nabla} \cdot \left(\frac{1}{\rho^{n+1}}\left(\boldsymbol{\nabla} P^{n+1}\right)\right) = \frac{\boldsymbol{\nabla} \cdot \boldsymbol{u}^*}{\Delta t} \tag{45}$$

3: Compute $\boldsymbol{u}^{n+1}$ (Corrector step):

$$\boldsymbol{u}^{n+1} = \boldsymbol{u}^* + \frac{\Delta t}{\rho^{n+1}}(-\boldsymbol{\nabla} P^{n+1}) \tag{46}$$

5.4. Viscous formulation

Ghost Fluid Method (GFM) has been proved to be advantageous in computing the pressure jump across the interface in the context of multiphase flows. Albeit this advantage, it becomes challenging to implement the formulations proposed in the literature [48] for this method in the presence and discretization of viscous terms. Thus, to this end, we have used the semi-implicit formulation proposed by Sussman et al. [49] for discretizing the viscous term. With this method, we can be second-order accurate in regions away from the liquid/gas interface and first-order accurate near the interface.

The viscous terms have profound effect only in the small scales of motion. And, our interest lies on simulating the complex, turbulent multiphase flow problems. Thus, it is considered that our choice of discretization of viscous term will not have significant impact on the results of global characteristics of atomization.

5.5. Time integration

The Navier-Stokes equations are solved using a one-step forward Euler scheme. The time step size Δt is determined based on a CFL condition similar to that of Kang et al. [48]. For a value of CFL = γ, the time steps

size is computed by satisfying the inequality

$$\Delta t \leq \frac{\gamma}{\left(\frac{(C_{\mathrm{CFL}}+V_{\mathrm{CFL}})\sqrt{(C_{\mathrm{CFL}}+V_{\mathrm{CFL}})^2+4(G_{\mathrm{CFL}})^2+4(S_{\mathrm{CFL}})^2}}{2}\right)} \tag{47}$$

where C_{CFL}, V_{CFL}, G_{CFL}, and S_{CFL} represent the CFL conditions based on convective, viscous, gravity, and surface tension (capillary) forces. Each of the terms are computed as

$$C_{\mathrm{CFL}} = \frac{\max(\mid u \mid)}{\Delta x} + \frac{\max(\mid v \mid)}{\Delta y} + \frac{\max(\mid w \mid)}{\Delta z}, \tag{48}$$

$$V_{\mathrm{CFL}} = \max\left(\frac{\mu_{\mathrm{liq}}}{\rho_{\mathrm{liq}}}, \frac{\mu_{\mathrm{gas}}}{\rho_{\mathrm{gas}}}\right)\left(\frac{2}{(\Delta x)^2} + \frac{2}{(\Delta x)^2} + \frac{2}{(\Delta z)^2}\right), \tag{49}$$

$$G_{\mathrm{CFL}} = \sqrt{\frac{\mid g_x \mid}{\Delta x}} + \sqrt{\frac{\mid g_y \mid}{\Delta y}} + \sqrt{\frac{\mid g_z \mid}{\Delta z}}, \text{ and} \tag{50}$$

$$S_{\mathrm{CFL}} = \sqrt{\frac{\sigma \max(\mid \kappa \mid)}{\rho_{\mathrm{gas}}(\Delta x)^2}} \tag{51}$$

where g is the acceleration due to gravity.

5.6. Overall solution procedure

Figure 13 gives the flowchart of the overall list of different routines and the steps in our solver coupled with MOF interface reconstruction and advection subroutines. The transport of phase-based and flow-based quantities are performed with the time step size determined based on the CFL criterion.

6. Validation tests

In this section, we assess the capability of the MOF method for simple two-phase flows. To that end, we present in this section two tests: a double shear layer dominated by convection and Rayleigh-Taylor instability test.

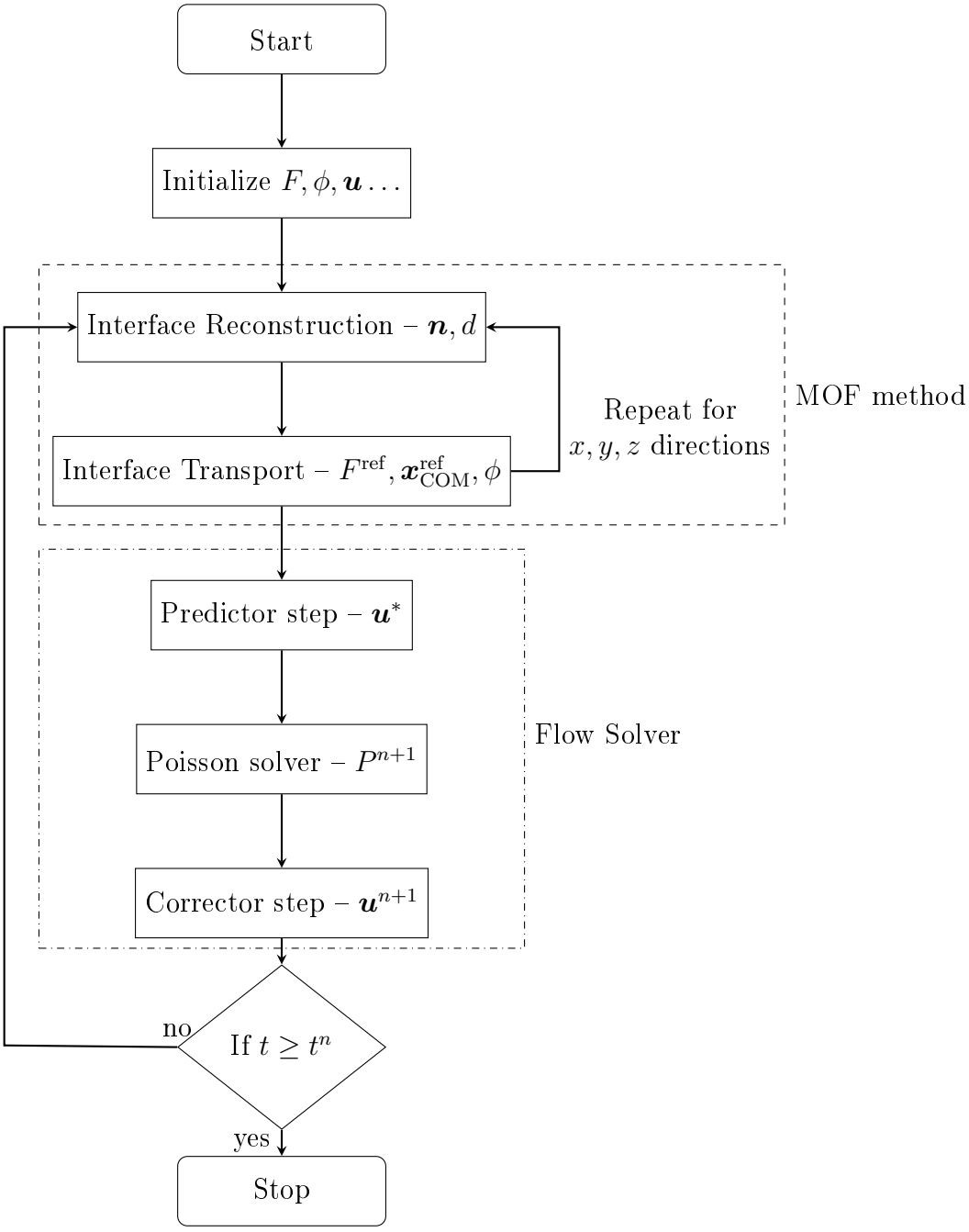

Figure 13: Solution procedure coupled with MOF interface reconstruction method.

6.1. Double shear layer

Numerical simulations of atomization process involves complex topological structures that need to be well captured in the domain. Moreover, there can arise a situation when liquid structures dominated by convective forces need to be reconstructed. Quite often in such convection dominated flow conditions, a non-negligible inaccuracy in the computation of liquid/gas interface normal during reconstruction can have this error propagating to the incorrect computation of density and subsequently to the incorrect computation of velocity. Vaudor [50] demonstrated that such inaccuracies in velocity computation often led to burst or sudden increase in velocity between adjacent time steps. Such bursts or intermittent shoot-ups (as it will be referred hereon) have an adverse effect on the results obtained from numerical simulation thereby leading to poor understanding of the physical process of atomization. This can be directly linked to the stability of the solution to the Navier-Stokes equations and by extension to that of the interface reconstruction numerical method.

As remarked in Section 2.2.2, inaccurate capture of under-resolved liquid structures in atomization process can lead to inaccuracies and instability in the solution to velocity and pressure field in the Navier-Stokes equations. It is important to test whether MOF method is stable and able to well capture these under-resolved liquid structures under convective conditions. To that end, we consider a $L \times L$ double shear layer configuration as shown in Figure 14 with $L = 0.003$ and $\delta = L/10$. The density ratio between liquid and gas is taken to be 1000. The viscous and surface tension forces are assumed to be many orders of magnitude smaller than the convective term, therefore, are neglected. Thus, the flow Reynolds number $\mathrm{Re} = \infty$ and liquid based Weber number $\mathrm{We} = \infty$. A *divergence free* initial velocity field is prescribed in the domain given as follows

$$u = A - 0.04 \cos\left(\frac{2\pi x}{L}\right)\left(\frac{L}{x}\right)\left(\frac{-2}{\delta}\right)\exp\left(-\frac{2y}{\delta}\right), \tag{52}$$

$$v = 0.04 \sin\left(\frac{2\pi x}{L}\right)\exp\left(-\frac{2y}{\delta}\right) \tag{53}$$

in which δ is the thickness of the liquid shear layer and the value for A is taken as

$$A = \begin{cases} 30\ , \text{ in gas phase} \\ 2\ , \text{ in liquid phase.} \end{cases} \tag{54}$$

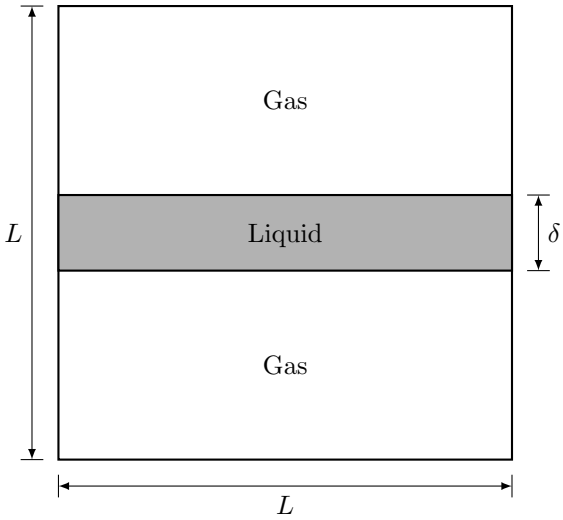

Figure 14: Configuration of a 2D double shear layer.

Five mesh resolutions are considered in this test case ranging from 32×32 to 512×512 and periodic boundary conditions are used along $x-$ and $y-$directions. The simulation is run until the physical time $t = 2 \times 10^{-3}$. The results shown for this test pertains to 128×128 mesh resolution for MOF and CLSVOF methods.

We present here results from three cases, first is MOF without *VOF restriction* (c.f. Section 2.2.2), second is CLSVOF without *VOF restriction*, and finally, CLSVOF with *VOF restriction*. To give more explanation, "without *VOF restriction*" means the presence of under-resolved liquid structures in the simulation domain while "with *VOF restriction*" means that these structures are deleted by the level set function using the criteria discussed in Section 2.2.2. Thus, the only difference between the second and third case is the presence of under-resolved liquid structures in the simulation domain. When such structures are not well captured, we should observe intermittent bursts/shoot-ups in the velocity field [50].

Due to the periodic boundary conditions, the total kinetic energy E_{kin} (sum of the kinetic energy of liquid and gas phase) must remain constant over time. Figure 15a shows the plot of the time evolution of the total kinetic energy for MOF method (black solid line) and CLSVOF method without *VOF restriction* (red dashed line) and with *VOF restriction* (blue dashdotted line). For all the three cases, the total kinetic energy is observed to remains

nearly constant. Howoever, there is a decrease observed towards the later simulation time. It is expected to have arisen from the numerical dissipation induced by the discretization schemes employed in our in-house Navier-Stokes solver ARCHER. An accurate capture of the under-resolved liquid structures can be observed from the non-presence of intermittent velocity bursts. Such velocity bursts often lead to fluctuations in the total kinetic energy. From Figure 15a, we can observe that the only case with such bursts is the CLSVOF method without *VOF restriction* (see also the inset plot in this figure) due to the inaccurate capture of these structures. In order to further investigate based on this this inference, we show the evolution of the maximum cell centered velocity field as a function of time in Figure 15b. This velocity is computed as

$$(\|\boldsymbol{u}^c\|_2)_{\max} = \sqrt{(u^c)^2 + (v^c)^2}. \tag{55}$$

As expected, once again the CLSVOF method without *VOF restriction* is

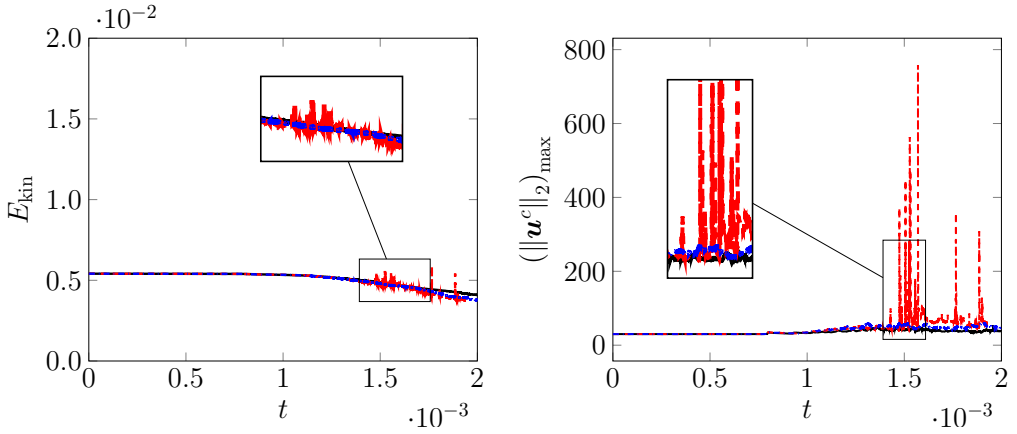

(a) Total kinetic energy (b) Maximum velocity magnitude

Figure 15: Time evolution of total kinetic energy and maximum cell centered velocity magnitude for 128×128 mesh resolution using MOF method without *VOF restriction* (——), CLSVOF method without *VOF restriction* (- - -), and CLSVOF method with *VOF restriction* (-·-·-).

experiencing large number of intermittent velocity bursts. Such bursts are not observed when using CLSVOF method with *VOF restriction* since the under-resolved structures are deleted. Furthermore, the MOF method without *VOF restriction* is also not having such shoot-ups. Thus, from these inferences, we can conclude that the sole reason for the presence of intermit-

tent velocity burst for the CLSVOF method without *VOF restriction* is due to inaccurate capture of under-resolved liquid structures.

Based on this conclusion, MOF method is able to well accurately capture the under-resolved liquid structures in multiphase flow simulations. Moreover, it is observed that MOF method is stable and able to handle the extreme convective flow conditions.

Finally, the phase interface and the contour of the magnitude of the cell centered velocity for two instantaneous time steps using MOF method and CLSVOF method without *VOF restriction* are shown respectively in Figures 16 and 17. In these figures, the solid line represents the liquid/gas interface. Although the surface tension force is neglected in our simulation, we still see a small number of detached liquid structures in the domain (c.f. Figure 17b). Such breakup is expected to have occurred due to the coarse mesh resolution employed for the simulation. As the mesh resolution increases, the number of such liquid structure detachments decreases. Furthermore, with the increasing mesh resolution, liquid filaments formed due to shear between liquid and gas phases, grow longer without artificial/numerical and premature breakup.

It is to be remarked that there is 0% mass loss in the domain when *VOF restriction* is deactivated while there is a mass loss of 3.19% when it is activated. Thus, MOF method is able to conserve mass and capture the under-resolved liquid structures without any bursts in the velocity.

6.2. Rayleigh-Taylor instability

Next, the Rayleigh-Taylor instability test is performed for the assessment of the MOF method in capturing the thin filaments and high curvature interfacial regions when coupled with Navier-Stokes equations. This test has been extensively studied in the literature, for example see [51, 52, 53]. However, these works did not consider effect due to surface tension. In recent studies [15, 18, 39], surface tension forces are considered. In this paper, we consider the configuration described in [39].

To this end, we consider a 1×4 domain containing two fluid phases that are separated by an interface. This interface is defined by the zero value of the level set given as

$$\phi(x, y) = y + A\cos(2\pi x) \tag{56}$$

where $A = 0.05$ is chosen for this test case. The density of the top fluid (denoted as fluid 1) is $\rho_1 = 1.225$ while that of the bottom fluid (denoted

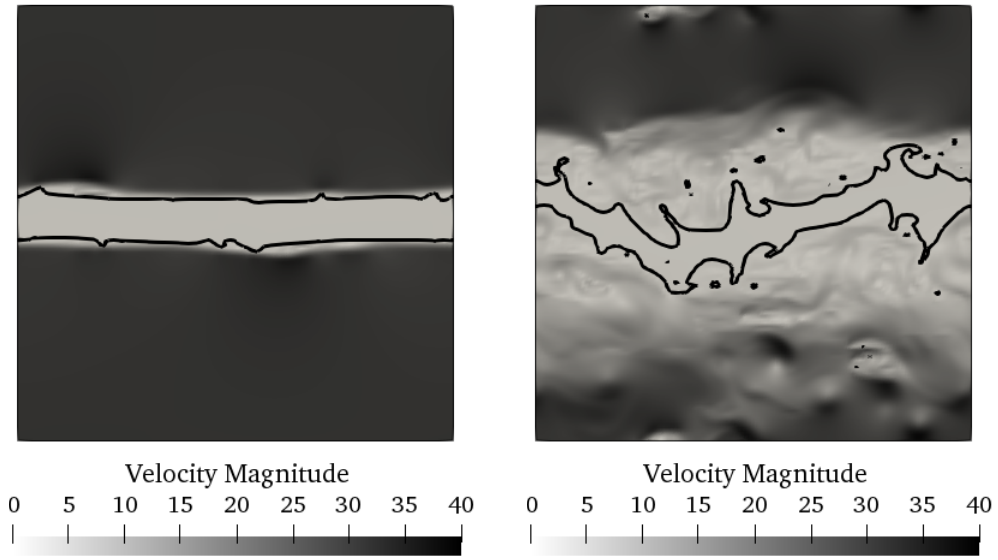

(a) $t = 1.07 \times 10^{-3}$ (b) $t = 2.00 \times 10^{-3}$

Figure 16: Phase interface (solid line) and contour of magnitude of velocity for double shear layer test using MOF method for 128×128 mesh resolution.

as fluid 2) is $\rho_2 = 0.1694$. The dynamic viscosities of the two fluids are same $\mu_1 = \mu_2 = 0.00313$. The surface tension is taken as $\sigma = 0.1337$. The acceleration due to gravity $g = 9.81\,\mathrm{m/s^2}$. Periodic boundary condition is considered along $x-$direction (horizontal direction) and wall boundary condition along $y-$direction (vertical direction). Four different mesh resolutions are considered ranging from 32×128 to 256×1024. The test case is run upto a physical time of $t = 1.2$.

Figure 18 shows the time evolution of the phase interface shape for the Rayleigh-Taylor instability test using 256×1024 mesh resolution. The results are in good agreement with that from the work of Desjardins and Pitsch [39, Figures 22 and 23] which was performed using a spectrally refined interface method with 512×2048 mesh resolution.

Figure 19 shows the fluid phase interfaces for all mesh resolutions for the time steps $t = 1.0, 1.1, 1.2$. The arrow in these figures indicates the increasing mesh resolutions considered in this work for this test case. The depth (in vertical $y-$direction) until which the fluid 1 goes into the fluid 2 is defined as

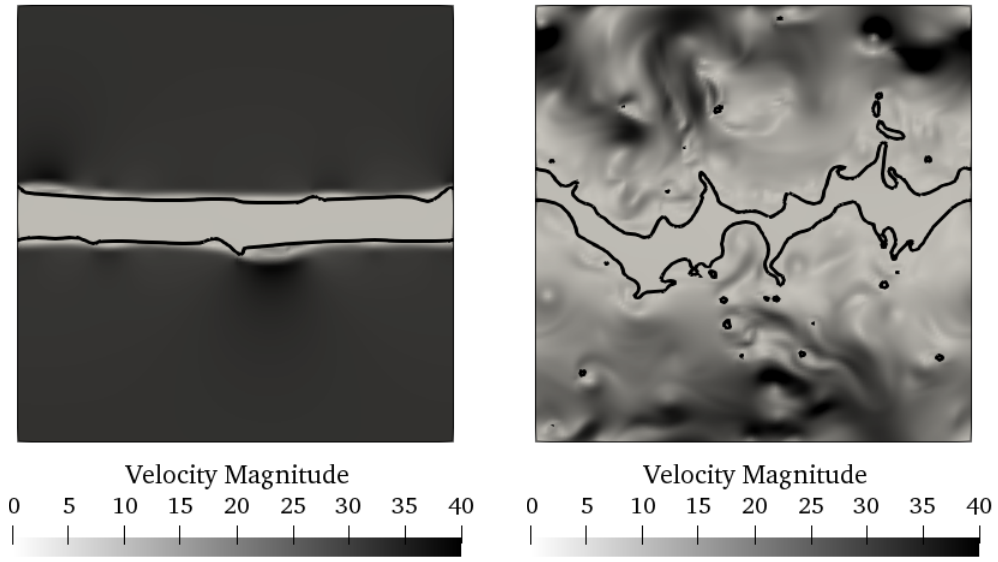

(a) $t = 1.07 \times 10^{-3}$ (b) $t = 1.96 \times 10^{-3}$

Figure 17: Phase interface (solid line) and contour of magnitude of velocity for double shear layer test using CLSVOF method for 128×128 mesh resolution.

the spike penetration within this work. The value of the spike penetration for the mesh resolution 256×1024 is used as reference solution for the purpose of comparisons. From this figure, it can be observed qualitatively that the spike penetration converges relatively faster towards the reference solution from the observation that the lines collapse as the mesh resolution is increased.

In order to quantify and validate this observation, we have computed an error estimate called spike penetration error. This is defined as the distance between the spike penetration for a given mesh resolution and the reference solution. This error estimate is then compared for various mesh resolutions over multiple time instants and is shown in Figure 20. A second-order convergence of the error can be observed in this figure for all the three time instants which validates the observation made from Figure 19 on faster convergence. With the increasing simulation time, more complex interfacial structures such as thin filaments and ligaments are formed thereby increasing the error towards the end of the simulation.

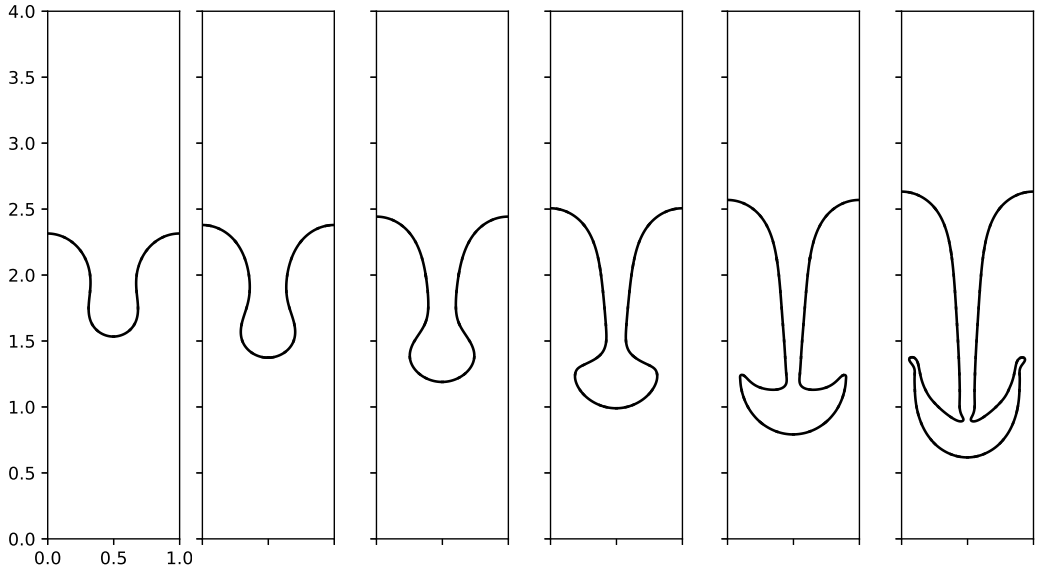

(a) $t = 0.7$ (b) $t = 0.8$ (c) $t = 0.9$ (d) $t = 1.0$ (e) $t = 1.1$ (f) $t = 1.2$

Figure 18: Time evolution of phase interface for Rayleigh-Taylor instability test using MOF method with 256×1024 mesh resolution.

7. Atomization of turbulent liquid diesel jet

Finally, we apply the MOF method to simulate turbulent atomization of round liquid diesel jet. The verification and validation tests presented in Sections 4 and 6 involve non-complex interface topologies, low Reynolds numbers, or flows dominated by convection. The fuel injection in gas turbines is often carried out under extreme conditions creating complex liquid structures and interface topologies. It is to be noted that the results presented in this section are solely for testing the potentialities of the MOF method rather than as reference results.

In order to validate the proposed MOF method for such interface topologies, a spatially evolving liquid jet turbulent atomization computation is performed. To that end, a turbulent liquid diesel jet is injected using a simple circular cross-sectional injector into a quiescent environment of gas. The jet upon penetration into the surroundings is disintegrated into ligaments and droplets upon action of shear and aerodynamic forces.

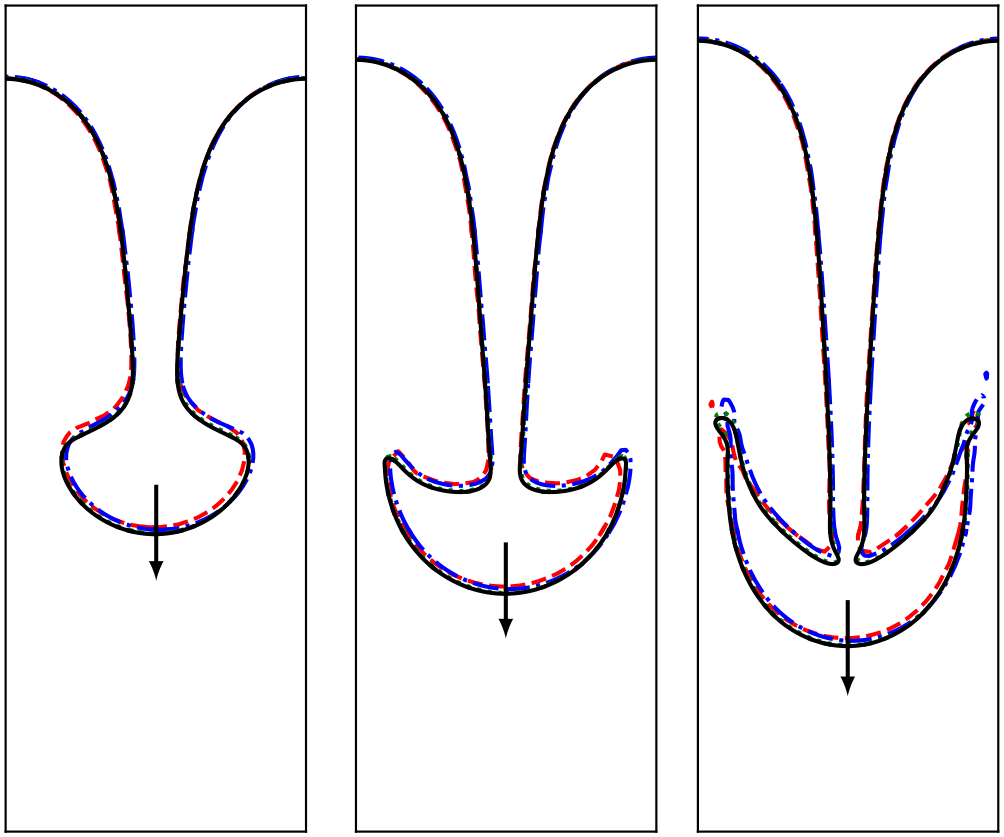

(a) $t = 1.0$ (b) $t = 1.1$ (c) $t = 1.2$

Figure 19: Fluid phase interface shape as a function of time for Rayleigh–Taylor instability test using MOF method with arrow indicating increasing mesh resolutions. 32×128 (- - -), 64×256 (-·-·-), 128×512 (·····), and 256×1024 (——).

7.1. Computational details

The computation has been performed in a domain of size $3D_j \times 3D_j \times 24D_j$ where D_j is the diameter of the injector of the liquid jet that is discretized using $128 \times 128 \times 1024$ structured Cartesian mesh resulting in $D_j/\Delta x = 42.74$. The mesh resolution has been chosen under the assumption that no secondary breakup occurs for the smallest droplet. It is to be remarked that although the employed mesh resolution might not capture all scales of motion in this turbulent flow, no sub-grid scale (SGS) models were used. It is however unclear whether these scales of motion will affect the global nature

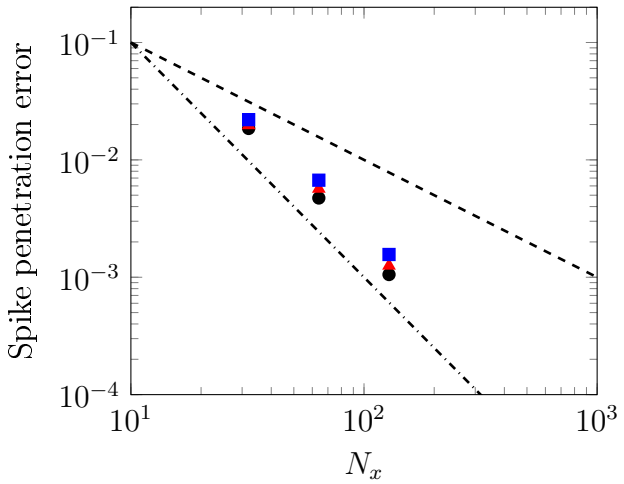

Figure 20: Spike penetration error: $t = 1.0$ (●); $t = 1.1$ (▲); $t = 1.2$ (■); first-order convergence line (- - -); second-order convergence line (-·-·-).

of the atomization analyzed in this case. Nevertheless, the objective of this section to demonstrate the ability of MOF method to simulate a complex turbulent engineering application. The characteristics of the jet and operating conditions are respectively given in Tables 4, 5 and 6. The jet Reynolds

Table 4: Characteristics of turbulent liquid jet.

Physical quantity	**Value**
Jet diameter (D_j)	100 µm
Mean jet velocity ($\overline{U}_j$)	100 m/s
Turbulent intensity (u')	$0.10\overline{U}_j$
Turbulent integral length scale (l_t)	$0.1D_j$

Table 5: Operating conditions summary.

Phase	ρ [kg/m^3]	μ [kg/ms]	σ [N/m]
Liquid	696	1.2×10^{-3}	0.06
Gas	25	1×10^{-5}	

number is expressed as $Re_j = \rho_j \overline{U}_j D_j / \mu_j$ and liquid based Weber number is expressed as $We = \rho_j \overline{U}_j^2 D_j / \sigma$. A fully developed turbulent pipe flow velocity

Table 6: Non-dimensional numbers for turbulent liquid jet atomization.

Non-dimensional number	**Value**
Jet Reynolds number (Re_j)	5800
Liquid Weber number (We)	11 600
Turbulent Reynolds number (Re_τ)	58
$D_j/\Delta x$	42.74
$l_t/\Delta x$	4

inlet is used for liquid phase inflow boundary condition. The turbulent inflow boundary conditions are generated using the synthetic turbulence method of Klein et al. [54] which consists of generating correlated random velocities with a prescribed length scale. In our study, we considered this length scale to be equal to the turbulent integral length scale l_t (c.f. Table 4). With the current mesh resolution, we have $l_t/\Delta x \approx 4$. The turbulent Reynolds number at injection $Re_\tau = \rho_j u' l_t/\mu_j = 58$.

The simulation is run upto a non-dimensional time $t^* = t\overline{U}_j/D_j = 20$ using our in-house code ARCHER [17, 33] in CRIANN supercomputing facility on 512 processors.

7.2. Atomization results

Figure 21 shows the instantaneous snapshots of the liquid jet at various times. It can be seen that the liquid jet interface experiences a lot of disturbances on its surface due to the turbulence causing the formation of 3D waves. These waves then roll-up thereby pinching the interface leading to detachment of ligaments and droplets from the liquid core. We can also observe that by the end of the computation, significant deformation of the liquid jet has resulted in numerous ligaments and droplets being detached from the liquid core.

To assess the ability of MOF method for this case, we compute the loss/gain of liquid volume in the domain over time. To this end, we define the volume lost/gained V_{lg} (depending on negative/positive value respectively) computed for each time step over the whole domain in the simulation as

$$V_{\mathrm{lg}}(t) = V_{\mathrm{total}}(t) - V_0 - V_{\mathrm{inlet}}(t), \tag{57}$$

where V_{total} is the total liquid volume in the domain at a particular time instant t, V_0 is the initialized liquid volume of the cylindrical jet cap of diameter

Figure 21: Time evolution of turbulent atomization of liquid diesel jet. $\Delta t^* = 2.5$ between each snapshot.

D_j and height $4\Delta x$ at $t = 0$, and V_{inlet} is the injected liquid volume computed using the amount of the flux of the volume entering the injector cross-section. Positive values for V_{lg} indicate gain in liquid mass while negative values indicate loss in liquid mass. The loss of volume in the domain is normalized

using the total volume of the domain ($V_{\text{domain}} = 3D_j \times 3D_j \times 24D_j$). The evolution of $V_{\text{lg}}/V_{\text{domain}}$ as a function of time is shown in Figure 22. With the volume loss in the order of 1.0×10^{-16} in the domain, the MOF method is able to conserve the liquid mass very satisfactorily even for this complex turbulent case.

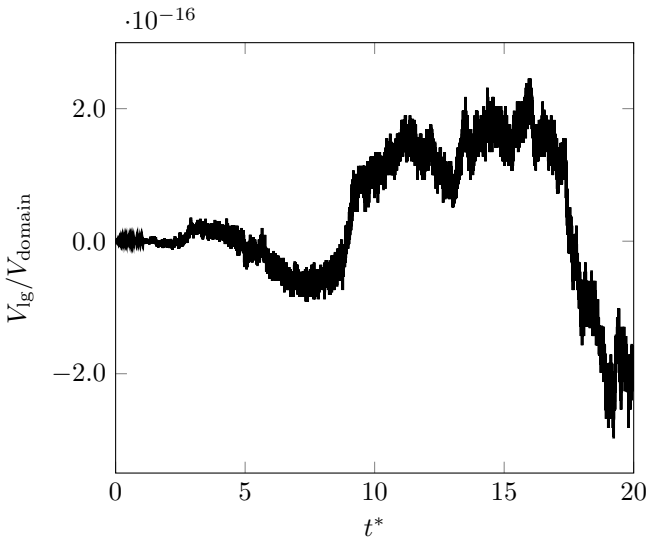

Figure 22: Conservation of liquid volume (normalized by total volume of domain) for turbulent atomization of liquid diesel jet.

8. Conclusions

A moment of fluid (MOF) interface reconstruction approach for simulating complex, turbulent multiphase flows has been developed and coupled with incompressible Navier-Stokes equations. This numerical moment based method uses liquid volume fraction and phase centroid for reconstruction of liquid/gas interface. The additional advantage that this method brings to the table is the accurate capturing of under-resolved interface topology. The core idea of the moment of fluid method is to reconstruct the interface in a volume conservative manner and by reducing the centroid defect to the minimum in each computational cell. This method has been subjected to various tests under multiple flow conditions and is shown to be performing with good results and relatively less error than a classical coupled level set volume of fluid approach. Finally, this method has been used to simulate

atomization of turbulent liquid diesel jet. For such a complex multiphase problem, the method is shown to perform very satisfactorily and the errors in the volume conservation is demonstrated to be small.

These small error estimates for the MOF method is due to well capture of the under-resolved regions. The coupled level set volume of fluid (CLSVOF) method is able to well capture the resolved liquid structures. New developments are planned to develop a hybrid coupled level set moment of fluid method, similar to that of Jemison et al. [23], that uses MOF method only for reconstructing under-resolved liquid structures while CLSVOF method for reconstructing resolved structures. The rationale behind this approach is to exploit the accurate interface reconstruction method of MOF with optimal computational resources requirement from CLSVOF method.

Acknowledgements

The funding for this project from the European Union's Horizon 2020 research and innovation programme under the Marie Skłodowska-Curie grant agreement N° 650676 is gratefully acknowledged. The authors wish to express gratitude to Dr. Antoine Lemoine, Dr. Alexandre Poux, Prof. Marcus Herrmann, Mr. Victor Chéron, and Mr. Alberto Remigi for useful discussions and comments during the MOF method development. We are also thankful to Mr. Karthik Kannan for his fruitful comments on a draft of this manuscript. The computing time at CRIANN (Centre Régional Informatique et d'Applications Numériques de Normandie) under the scientific project No. 2003008 and at GENCI-[TGCC/CINES/IDRIS] (Grant2019-2613) are also gratefully acknowledged.

Appendix A. Finding reference phase centroids

The computation of the coordinates of reference phase centroid in each mixed computationl cell is performed using a triangulation method. Let us consider the following configuration of a two-dimensional (2D) mixed cell shown in Figure A.23. The computation of the centroid of liquid phase (dark fluid) is explained below. The computation of the gas phase centroid follows identically.

It is to be remarked that the computation of the phase centroids require the coordinates of the points on the computational cell faces at which the 2D interface line (3D interface plane) intersects. There are four steps involved

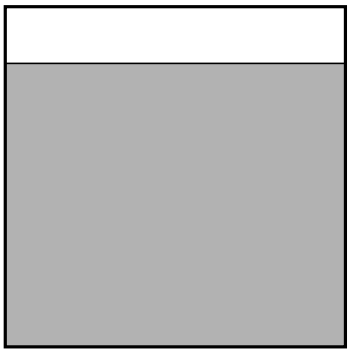

Figure A.23: Configuration of mixed cell for phase centroid computation.

in the procedure to compute the liquid phase centroid. They are as follows and are illustrated in Figure A.24.

(a) First, determine the coordinates of the barycenter of the liquid phase in the computational cell (c.f. Figure A.24a). The barycentre of the liquid phase is computed using coordinates of the interface-cell intersection points and coordinates of the cell corners in the liquid phase.

(b) Next, triangulate the liquid packet with barycenter of the liquid phase as one of the common vertex of the triangles and compute the volumes of each triangulated element V_{it} (c.f. Figure A.24b). The faces of each triangulated element is represented by dashed line.

(c) Compute the barycenter of each of these triangulated elements (c.f. Figure A.24c) using a simple formula given as

$$\boldsymbol{x}_{\mathrm{barycenter}} = \frac{\sum_{\mathrm{iv}=1}^{\mathrm{NV}} \boldsymbol{x}_{\mathrm{iv}}}{\mathrm{NV}} \tag{A.1}$$

where NV is the number of vertices of the triangulated elements (in this case NV = 3 for triangular elements while NV = 4 for tetrahedral elements in 3D)

(d) Compute the centroid of the liquid phase as the weighted average of the barycenter of each triangulated element with their volume of weights (c.f.

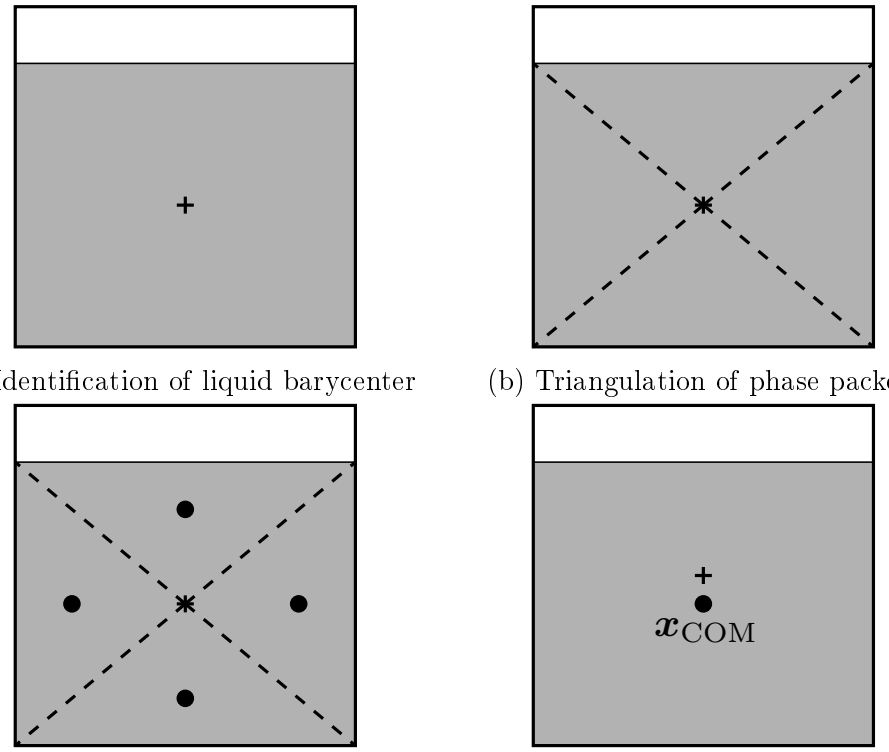

(a) Identification of liquid barycenter

(b) Triangulation of phase packet

(c) Barycenter computation for each triangulated phase pakcet

(d) Weighted average of barycenter

Figure A.24: Step-by-step procedure for computation of phase centroid.

Figure A.24d), i.e.,

$$\boldsymbol{x}_{\mathrm{COM}} = \frac{\sum_{\mathrm{it}=1}^{\mathrm{NT}} \boldsymbol{x}_{\mathrm{barycenter}_{\mathrm{it}}} V_{\mathrm{it}}}{\sum_{\mathrm{it}=1}^{\mathrm{NT}} V_{\mathrm{it}}} \tag{A.2}$$

where NT is the total number of triangulated elements in the computational cell.

The extension of this procedure to 3D is performed in a similar fashion as described above along with the triangulation of the liquid/gas interface plane for creating tetrahedron.

References

[1] M. Gorokhovski, M. Herrmann, Modeling primary atomization, Annual Review of Fluid Mechanics 40 (2008) 343–366. URL: https://doi.org/10.1146/annurev.fluid.40.111406.102200. doi:10.1146/annurev.fluid.40.111406.102200.

[2] E. Aulisa, S. Manservisi, R. Scardovelli, S. Zaleski, A geometrical area-preserving Volume-of-Fluid advection method, Journal of Computational Physics 192 (2003) 355–364. URL: https://doi.org/10.1016/j.jcp.2003.07.003. doi:10.1016/j.jcp.2003.07.003.

[3] J. Hernández, J. López, P. Gómez, C. Zanzi, F. Faura, A new volume of fluid method in three dimensions–Part I: Multidimensional advection method with face-matched flux polyhedra, International Journal for Numerical Methods in Fluids 58 (2008) 897–921. URL: https://doi.org/10.1002/fld.1776. doi:10.1002/fld.1776.

[4] J. López, C. Zanzi, P. Gómez, F. Faura, J. Hernández, A new volume of fluid method in three dimensions–Part II: Piecewise-planar interface reconstruction with cubic-Bézier fit, International Journal for Numerical Methods in Fluids 58 (2008) 923–944. URL: https://doi.org/10.1002/fld.1775. doi:10.1002/fld.1775.

[5] M. Owkes, O. Desjardins, A mass and momentum conserving unsplit semi-Lagrangian framework for simulating multiphase flows, Journal of Computational Physics 332 (2017) 21–46. URL: https://doi.org/10.1016/j.jcp.2016.11.046. doi:10.1016/j.jcp.2016.11.046.

[6] E. Aulisa, S. Manservisi, R. Scardovelli, S. Zaleski, Interface reconstruction with least-squares fit and split advection in three-dimensional cartesian geometry, Journal of Computational Physics 225 (2007) 2301–2319. URL: https://doi.org/10.1016/j.jcp.2007.03.015. doi:10.1016/j.jcp.2007.03.015.

[7] P. Cifani, W. R. Michalek, G. J. M. Priems, J. G. M. Kuerten, C. W. M. van der Geld, B. J. Geurts, A comparison between the surface compression method and an interface reconstruction method for the VOF approach, Computers & Fluids 136 (2016) 421–435. URL: https://doi.org/10.1016/j.compfluid.2016.06.026. doi:10.1016/j.compfluid.2016.06.026.

[8] H. Grosshans, R.-B. Szász, L. Fuchs, Development of a Combined VOF-LPT Method to Simulate Two-phase Flows in Various Regimes, in: 7th International Symposium on Turbulence and Shear Flow Phenomena, TSFP7, Ottawa, Canda, 2011.

[9] A. Orazzo, I. Lagrange, J.-L. Estivalézes, D. Zuzio, A VoF-Based Consistent Mass-Momentum Transport for Two-Phase Flow Simulations, in: Proceedings of the ASME 2017 Fluids Engineering Division Summer Meeting, FEDSM2017, July 30-August 3, 2017, Waikoloa, Hawaii, USA, 2017, pp. 1–11. doi:10.1115/FEDSM2017-69190.

[10] S. Osher, J. A. Sethian, Fronts propagating with curvature-dependent speed: Algorithms based on Hamilton-Jacobi formulations, Journal of Computational Physics 79 (1988) 12–49. URL: https://doi.org/10.1016/0021-9991(88)90002-2. doi:10.1016/0021-9991(88)90002-2.

[11] S. Osher, R. Fedkiw, Level Set Methods and Dynamic Implicit Surfaces, Springer, 2003.

[12] E. Olsson, G. Kreiss, A conservative level set method for two phase flow, Journal of Computational Physics 210 (2005) 225–246. URL: https://doi.org/10.1016/j.jcp.2005.04.007. doi:10.1016/j.jcp.2005.04.007.

[13] O. Desjardins, V. Moureau, H. Pitsch, An accurate conservative level set/ghost fluid method for simulating turbulent atomization, Journal of Computational Physics 227 (2008) 8395–8416. URL: https://doi.org/10.1016/j.jcp.2008.05.027. doi:10.1016/j.jcp.2008.05.027.

[14] R. Chiodi, O. Desjardins, A reformulation of the conservative level set reinitialization equation for accurate and robust simulation of complex multiphase flows, Journal of Computational Physics 343 (2017) 186–200. URL: https://doi.org/10.1016/j.jcp.2017.04.053. doi:10.1016/j.jcp.2017.04.053.

[15] M. Herrmann, A balanced force refined level set grid method for two-phase flows on unstructured flow solver grids, Journal of Computational Physics 227 (2008) 2674–2706. URL: https://doi.org/10.1016/j.jcp.2007.11.002. doi:10.1016/j.jcp.2007.11.002.

[16] M. Sussman, E. G. Puckett, A Coupled Level Set and Volume-of-Fluid Method for Computing 3D and Axisymmetric Incompressible Two-Phase Flows, Journal of Computational Physics 162, (2000) 301–337. URL: https://doi.org/10.1006/jcph.2000.6537. doi:10.1006/jcph.2000.6537.

[17] T. Ménard, S. Tanguy, A. Berlemont, Coupling level set/VOF/ghost fluid methods: Validation and application to 3D simulation of the primary break-up of a liquid jet, International Journal of Multiphase Flow 33 (2007) 510–524. URL: https://doi.org/10.1016/j.ijmultiphaseflow.2006.11.001. doi:10.1016/j.ijmultiphaseflow.2006.11.001.

[18] V. Le Chenadec, H. Pitsch, A 3D Unsplit Forward/Backward Volume-of-Fluid Approach and Coupling to the Level Set Method, Journal of Computational Physics 233 (2013) 10–33. URL: https://doi.org/10.1016/j.jcp.2012.07.019. doi:10.1016/j.jcp.2012.07.019.

[19] H. T. Ahn, M. Shashkov, Multi-material interface reconstruction on generalized polyhedral meshes, Journal of Computational Physics 226 (2007) 2096–2132. URL: https://doi.org/10.1016/j.jcp.2007.06.033. doi:10.1016/j.jcp.2007.06.033.

[20] V. Dyadechko, M. Shashkov, Reconstruction of multi-material interfaces from moment data, Journal of Computational Physics 227 (2008) 5361–5384. URL: https://doi.org/10.1016/j.jcp.2007.12.029. doi:10.1016/j.jcp.2007.12.029.

[21] H. T. Ahn, M. Shashkov, Adaptive moment-of-fluid method, Journal of Computational Physics 228 (2009) 2792–2821. URL: https://doi.org/10.1016/j.jcp.2008.12.031. doi:10.1016/j.jcp.2008.12.031.

[22] S. P. Schofield, M. A. Christon, V. Dyadechko, R. V. Garimella, R. B. Lowrie, B. K. Swartz, Multi-material incompressible flow simulation using the moment-of-fluid method, International Journal for Numerical Methods in Fluids 63 (2010) 931–952. URL: https://doi.org/10.1002/fld.2108. doi:10.1002/fld.2108.

[23] M. Jemison, E. Loch, M. Sussman, M. Shashkov, M. Arienti, M. Ohta, Y. Wang, A Coupled Level Set-Moment of Fluid Method for Incompress-

ible Two-Phase Flows, Journal of Scientific Computing 54 (2013) 454–491. URL: https://doi.org/10.1007/s10915-012-9614-7. doi:10.1007/s10915-012-9614-7.

[24] G. Li, Y. Lian, Y. Guo, M. Jemison, M. Sussman, T. Helms, M. Arienti, Incompressible multiphase flow and encapsulation simulations using the moment-of-fluid method, International Journal for Numerical Methods in Fluids 79 (2015) 456–490. URL: https://doi.org/10.1002/fld.4062. doi:10.1002/fld.4062.

[25] A. Asuri Mukundan, T. Ménard, A. Berlemont, J. C. Brändle de Motta, Interface reconstruction method for multiphase flows in under-resolved regions, in: Proceedings of the 10th International Conference on Computational Fluid Dynamics ICCFD10 2018, 9–13 July, Barcelona, Spain, 2018. URL: https://www.iccfd.org/iccfd10/proceedings.html.

[26] A. Asuri Mukundan, T. Ménard, A. Berlemont, J. C. Brändle de Motta, Numerical study of interface reconstruction method in under-resolved regions of the flow for liquid jet primary breakup, in: Proceedings of the ICLASS 2018, 14th Triennial International Conference on Liquid Atomization and Spray Systems, July 22-26, Chicago, IL, USA, 2018. URL: http://ilasseurope.org/events/iclass-2018/.

[27] A. Asuri Mukundan, T. Ménard, A. Berlemont, J. C. Brändle de Motta, A comparative study of dns of airblast atomization using clsmof and clsvof methods, in: Proceedings of the ILASS Europe, 29th Annual Conference on Liquid Atomization and Spray Systems, September 2-4, Paris, France, 2019, 2019.

[28] M. B. Freiss, J. Breil, P.-H. Maire, M. Shashkov, A Multi-Material CCALE-MOF Approach in Cylindrical Geometry, Communications in Computational Physics 15 (2014) 330–364. URL: https://doi.org/10.4208/cicp.190912.080513a. doi:10.4208/cicp.190912.080513a.

[29] S. Galera, J. Breil, P.-H. Maire, A 2D unstructured multi-material Cell-Centered Arbitrary Lagrangian–Eulerian (CCALE) scheme using MOF interface reconstruction, Computers & Fluids 46 (2011) 237–244. URL: https://doi.org/10.1016/j.compfluid.2010.09.038. doi:10.1016/j.compfluid.2010.09.038.

[30] J. Breil, T. Harribey, P.-H. Maire, M. Shashkov, A multi-material ReALE method with MOF interface reconstruction, Computers & Fluids 83 (2013) 115–125. URL: http://dx.doi.org/10.1016/j.compfluid.2012.08.015. doi:10.1016/j.compfluid.2012.08.015.

[31] A. Lemoine, S. Glockner, J. Breil, Moment-of-fluid analytic reconstruction on 2D Cartesian grids, Journal of Computational Physics 328 (2017) 131–139. URL: https://doi.org/10.1016/j.jcp.2016.10.013. doi:10.1016/j.jcp.2016.10.013.

[32] S. Tanguy, A. Berlemont, Application of a level set method for simulation of droplet collisions, International Journal of Multiphase Flow 31 (2005) 1015–1035. URL: https://10.1016/j.ijmultiphaseflow.2005.05.010. doi:10.1016/j.ijmultiphaseflow.2005.05.010.

[33] G. Vaudor, T. Ménard, W. Aniszewski, M. Doring, A. Berlemont, A consistent mass and momentum flux computation method for two phase flows. Application to atomization process, Computers & Fluids 152 (2017) 204–216. URL: https://doi.org/10.1016/j.compfluid.2017.04.023. doi:10.1016/j.compfluid.2017.04.023.

[34] G. D. Weymouth, D. K.-P. Yue, Conservative Volume-of-Fluid method for free-surface simulations on Cartesian-grids, Journal of Computational Physics 229 (2010) 2853–2865. URL: https://doi.org/10.1016/j.jcp.2009.12.018. doi:10.1016/j.jcp.2009.12.018.

[35] D. Gueyffier, A. Nadim, R. Scardovelli, S. Zaleski, Volume-of-Fluid Interface Tracking with Smoothed Surface Stress Methods for Three-Dimensional Flows, Journal of Computational Physics 152 (1999) 423–456. URL: https://doi.org/10.1006/jcph.1998.6168. doi:10.1006/jcph.1998.6168.

[36] R. Fletcher, Practical Methods of Optimization, 2nd edition ed., John Wiley & Sons, 1987.

[37] A. Björck, Numerical Methods for Least Squares Problems, SIAM, 1996. URL: https://doi.org/10.1137/1.9781611971484. doi:10.1137/1.9781611971484.

[38] J. López, J. Hernández, P. Gómez, F. Faura, A volume of fluid method based on multidimensional advection and spline interface reconstruction,

Journal of Computational Physics 195 (2004) 718–742. URL: https://doi.org/10.1016/j.jcp.2003.10.030. doi:10.1016/j.jcp.2003.10.030.

[39] O. Desjardins, H. Pitsch, A spectrally refined interface approach for simulating multiphase flows, Journal of Computational Physics 228 (2009) 1658–1677. URL: https://doi.org/10.1016/j.jcp.2008.11.005. doi:10.1016/j.jcp.2008.11.005.

[40] D. Enright, R. Fedkiw, J. Ferziger, I. Mitchell, A Hybrid Particle Level Set Method for Improved Interface Capturing, Journal of Computational Physics 183 (2002) 83–116. URL: https://doi.org/10.1006/jcph.2002.7166. doi:10.1006/jcph.2002.7166.

[41] R. J. LeVeque, High-Resolution Conservative Algorithms for Advection in Incompressible Flow, SIAM Journal on Numerical Analysis 33 (1996) 627–665. URL: https://doi.org/10.1137/0733033. doi:10.1137/0733033.

[42] B. Duret, G. Luret, J. Réveillon, T. Ménard, A. Berlemont, F.-X. Demoulin, DNS analysis of turbulent mixing in two-phase flows, International Journal of Multiphase Flow 40 (2012) 93–105. URL: https://doi.org/10.1016/j.ijmultiphaseflow.2011.11.014. doi:10.1016/j.ijmultiphaseflow.2011.11.014.

[43] R. Canu, S. Puggelli, M. Essadiki, B. Duret, T. Ménard, M. Massot, J. Réveillon, F. Demoulin, Where does the droplet size distribution come from?, International Journal of Multiphase Flow 107 (2018) 230–245. URL: https://doi.org/10.1016/j.ijmultiphaseflow.2018.06.010. doi:10.1016/j.ijmultiphaseflow.2018.06.010.

[44] J. Cousin, T. Ménard, A. Berlemont, S. Grout, Primary breakup simulation of a liquid jet discharged by a low-pressure compound nozzle, Computers & Fluids 63 (2012) 165–173. URL: http://dx.doi.org/10.1016/j.compfluid.2012.04.013. doi:10.1016/j.compfluid.2012.04.013.

[45] B. Duret, J. Réveillon, T. Ménard, F. X. Demoulin, Improving primary atomization modeling through DNS of two-phase flows, International Journal of Multiphase Flow 55 (2013) 130–137. URL: https://

doi.org/10.1016/j.ijmultiphaseflow.2013.05.004. doi:10.1016/j.ijmultiphaseflow.2013.05.004.

[46] R. Fedkiw, T. Aslam, B. Merriman, S. Osher, A Non-oscillatory Eulerian Approach to Interfaces in Multimaterial Flows (the Ghost Fluid Method), Journal of Computational Physics 152 (1999) 457–492. URL: https://doi.org/10.1006/jcph.1999.6236. doi:10.1006/jcph.1999.6236.

[47] M. Rudman, A volume-tracking method for incompressible multifluid flows with large density variations, International Journal for Numerical Methods in Fluids 28 (1998) 357–378. URL: http://onlinelibrary.wiley.com/doi/10.1002/(SICI)1097-0363(19980815)28:2%3C357::AID-FLD750%3E3.0.CO;2-D/epdf. doi:10.1002/(SICI)1097-0363(19980815)28:2<357::AID-FLD750>3.0.CO;2-D.

[48] M. Kang, R. Fedkiw, X. D. Liu, A Boundary Condition Capturing Method for Multiphase Incompressible Flow, Journal of Scientific Computing 15 (2000) 323–360. URL: https://doi.org/10.1023/A:1011178417620. doi:10.1023/A:1011178417620.

[49] M. Sussman, K. M. Smith, M. Y. Hussaini, M. Ohta, R. Zhi-Wei, A sharp interface method for incompressible two-phase flows, Journal of Computational Physics 221 (2007) 469–505. URL: https://doi.org/10.1016/j.jcp.2006.06.020. doi:10.1016/j.jcp.2006.06.020.

[50] G. Vaudor, Atomisation assistée par un cisaillement de l' écoulement gazeux. Développement et validation, Ph.D. thesis, University de Rouen Normandie, 2015. URL: http://www.coria.fr/spip.php?article1034&titre_mot=these&lang=en.

[51] A. Prosperetti, Viscous effects on small-amplitude surface waves, Physics of Fluids 19 (1976) 195–203. URL: https://doi.org/10.1063/1.861446. doi:10.1063/1.861446.

[52] R. Menikoff, R. C. Mjolsness, D. H. Sharp, C. Zemach, B. J. Doyle, Initial value problem for Rayleigh-Taylor instability of viscous fluids, Physics of Fluids 21 (1978) 1674–1687. URL: https://doi.org/10.1063/1.862107. doi:10.1063/1.862107.

[53] A. Prosperetti, Motion of two superposed viscous fluids, Physics of Fluids 24 (1981) 1217–1223. URL: https://doi.org/10.1063/1.863522. doi:10.1063/1.863522.

[54] M. Klein, A. Sadiki, J. Janicka, A digital filter based generation of inflow data for spatially developing direct numerical or large eddy simulations, Journal of Computational Physics 186 (2003) 652–665. URL: https://doi.org/10.1016/S0021-9991(03)00090-1. doi:10.1016/S0021-9991(03)00090-1.